

# Universal analytical modeling of coated plasmonic particles

Nikolai G. Khlebtsov<sup>1,2,\*</sup>, Sergey V. Zarkov<sup>1,3</sup>

<sup>1</sup>Institute of Biochemistry and Physiology of Plants and Microorganisms, "Saratov Scientific Centre of the Russian Academy of Sciences," 13 Prospekt Entuziastov, Saratov 410049, Russia

<sup>2</sup>Saratov State University, 83 Ulitsa Astrakhanskaya, Saratov 410012, Russia

<sup>3</sup>Institute of Precision Mechanics and Control, "Saratov Scientific Centre of the Russian Academy of Sciences," 24 Ulitsa Rabochaya, Saratov 410028, Russia

\*To whom correspondence should be addressed. E-mail: (NGK) [khlebtsov@ibppm.ru](mailto:khlebtsov@ibppm.ru)

## RECEIVED DATE

**Abstract.** From a structural point of view, plasmonic nanoparticles are always at least two-layer structures with a dielectric layer of stabilizing, targeting, fluorescent, Raman, or other functional molecules, often embedded in a matrix such as porous silica. To optimize the optical properties of such bioconjugates, one needs efficient analytical models based on simple physical ideas and with reasonable accuracy comparable to rigorous numerical methods requiring significant computer resources. Here, we present such type models based on a combination of the modal expansion method (MEM) and the dipole equivalence method (DEM). The MEM+DEM approach makes it possible to use the MEM parameters of the original metal particles and does not require additional numerical calculations to build models for bilayered or multilayered conjugates. Our analytical solutions depend on the particle shape, the shell thickness, and the shell refractive index, regardless of the particle size and the metal's nature. To illustrate the universality of our method, we calculate extinction and scattering spectra of gold and silver nanorods, nanodiscs, triangle nanoprisms, bicones, and bipyramids with a dielectric coating thickness from 0 to 30 nm. For the main plasmonic peaks, we found excellent agreement between our analytical method and numerical simulations performed with COMSOL, except for some disagreement between MEM and COMSOL solutions for bicones with small rounding radii. This drawback of MEM for coated particles is explained by the unusual local field

distribution with strong localization near the particle tips. To fix the point, we propose a factorized version of MEM that brings analytical spectra of coated bicones and bipyramids in excellent agreement with numerical counterparts. Due to the simplicity and reasonable accuracy of the MEM+DEM analytical models, they can help apply machine learning to predict various plasmonic responses such as light absorption, scattering, SERS, and metal-enhanced fluorescence.

**KEYWORDS:** gold and silver nanoparticles, coated nanoparticles, surface plasmon resonance, modal expansion, dipole equivalence method, T-matrix, COMSOL

## 1. Introduction

Modern methods of chemical synthesis<sup>1</sup> make it possible to obtain gold and silver nanoparticles (NPs) with precise control of their size, shape, and structure. The resulting NPs should be stabilized and functionalized with suitable surface ligands for biomedical applications.<sup>2-4</sup> NPs obtained by laser ablation<sup>5</sup> are chemically pure, but in biological environments, they will immediately aggregate if their surface is not coated with a stabilizer. Functionalization of NPs provides desirable properties for many promising applications, such as biosensing,<sup>6</sup> cardiovascular<sup>7</sup> therapy, photodynamic and photothermal<sup>8</sup> cancer therapy,<sup>9,10</sup> gene<sup>11</sup> and drug<sup>12</sup> delivery, enhancing adjuvant properties and protection of immune system cells,<sup>13</sup> etc. In the case of "green synthesis,"<sup>14</sup> the resulting NPs are always stabilized by the components of the reaction mixture after the synthesis is completed. The most well-known stabilizers are hexadecyltrimethylammonium bromide (CTAB) bilayer on the surface of gold nanorods. (AuNRs)<sup>15</sup> and stealth-immune coating by m-PEF-SH.<sup>13</sup> Thus, in the real world, stabilized and functionalized NPs are always at least bilayer particles with a plasmonic core and a dielectric shell. Therefore, their plasmonic properties differ from those of the original bare NPs.

Although current numerical methods can simulate plasmonic properties of NPs for almost arbitrary geometry,<sup>16</sup> such simulations may require significant computer resources for real polydisperse and polymorphic colloids. From the experimental point of view, it would be

desirable to have simple yet accurate analytical approximations based on clear physical ideas capable of predicting layered NP colloids' plasmonic properties with a common desktop PC just *in situ*. To meet this goal, we proposed<sup>17</sup> a combination of the improved electrostatic approximation (IEA)<sup>18</sup> with the dipole equivalence method (DEM)<sup>19</sup> for coated gold and silver spheroids. However, the spheroid is a convenient but simplified model just to account for basic shape effects.

Here, we propose a universal analytical model for coated plasmonic particles using a combination of the modal expansion method (MEM) developed recently by Yu *et al.*<sup>20</sup> with DEM. It should be emphasized that our analytical approach does not require any additional numerical calculations except for those for bare metal NPs. Our solution is described by four simple functions depending on a generalized aspect ratio, the shell thickness, and its refractive index for a specific particle shape. Moreover, the proposed analytical model can be easily extended to multilayer coating. To illustrate the universal possibilities of our method, we calculate extinction and scattering spectra of gold and silver nanorods (NRs), nanodiscs (NDs), triangle nanoprisms (NTs), bicones (BCs), and bipyramids (BPs). The accuracy of the MEM+DEM approach is examined with benchmark COMSOL simulations. We found excellent agreement between numerical and analytical methods in predicting the amplitude and spectral position of main localized plasmon resonance (LPR) peaks for rods, disks, and prisms. However, we discovered notable disagreement between MEM and COMSOL solutions for coated bicones and bipyramids. This disagreement is explained by the unusual local field distribution inside such NPs with strong localization near the particle tips. Such localization violates the dipole physical picture behind the DEM method. We propose a factorized version of MEM that brings analytical spectra of coated bicones and bipyramids in excellent agreement with numerical counterparts.

## 2. Methods

We used a commercial package COMSOL Multiphysics 5.1 (Wave Optics module) for benchmark electrodynamic simulations in standard 3D and new 2.5D<sup>21</sup> options. The latter ensures considerable computational savings regarding memory and processing time due to expanding all fields in the cylindrical harmonics and treating each harmonic independently.<sup>22</sup> This accelerates the computation speed considerably, thus making the random orientation averaging available with acceptable CPU time.

Our T-matrix method codes<sup>23</sup> (TMM) provide the fastest calculations for randomly oriented ensembles but only apply to homogeneous axially symmetrical NPs. In this work, we used 3D and 2.5D COMSOL calculations as benchmarks for MEM+DEM and TMM codes to check the accuracy of COMSOL simulations for bare NPs.

### 3. Modal expansion method for coated particles

#### 3.1. Models

Figure 1 shows five NP models that are described by a characteristic size  $L$ , a generalized aspect ratio  $AR$ , and the complex metal permittivity  $\varepsilon_1$ . A homogeneous coating (Figure 1B) is characterized by a constant shell thickness  $s$  and permittivity  $\varepsilon_2$ ; a homogeneous and host medium is characterized by a dielectric function  $\varepsilon_m$  (water in this work). The dielectric functions of gold and silver were calculated by tabulated data<sup>24</sup> and by a spline described in the Supporting Information file (SI, Section S1), respectively. We aim to examine the MEM+DEM model vs COMSOL simulations, so we used bulk optical constants without any size correction. Regarding the Drude model<sup>25,26</sup> the bulk dielectric functions can be easily corrected to account for known contributions from radiation damping,<sup>27</sup> surface electron scattering<sup>28,29</sup> and chemical interface damping.<sup>30-32</sup>

The SI file gives details of the particle shape geometries and explicit formulas for the core and total particle volumes (Section S2). For example, the core and total volumes of NRs with semispherical ends are equal to  $V_i = L_i^3 \pi (3AR_i - 1) / (12AR_i^3)$  and are characterized by the radii of

equivolume spheres  $R_{iev} = \sqrt[3]{3V_i/4\pi}$ , where indices  $i=1,2$  stand for core and shell, respectively,  $L_1 \equiv L$ ,  $AR_1 = AR$ ,  $L_2 = L + 2s$ ,  $AR_2 = (L + 2s)/(d + 2s)$ .

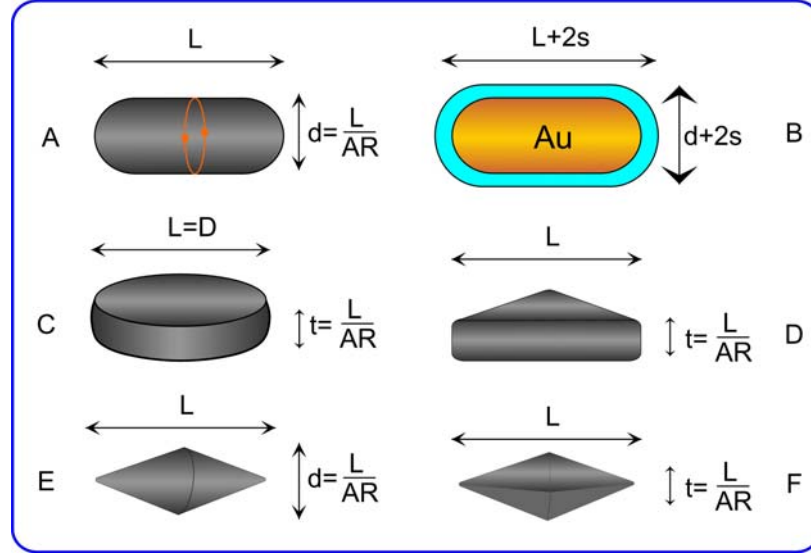


**Figure 1.** Geometrical models for five particle morphologies are characterized by the characteristic length  $L$  and a generalized aspect ratio  $AR$ . Panel B illustrates NP coating with a dielectric shell of a constant thickness  $s$ . NRs have hemispherical caps at the tips (A); NDs have semicircular edge profile (C); NTs have smooth edges with rounding radius  $(L+t)/40$  (D); BCs have rounded tips and circular base edge with rounding radii  $d/40$  and  $d/100$ , respectively, (E); BPs have pentagonal smooth base and rounded tips as indicated in ESI file.

### 3.2 Polarizability of coated metal particles in MEM

In MEM, the particle polarizability is expanded in terms of electrostatic eigenvalues

$$\alpha(\lambda) = \frac{1}{4\pi} \sum_j \bar{V}_j \left[ \frac{\epsilon_m}{\epsilon_1 - \epsilon_m} - \frac{1}{\eta_j - 1} - A_j \right]^{-1}, \quad (1)$$

$$A_j = a_{j2}x^2 + i \frac{4\pi^2 \bar{V}_j}{3L^3} x^3 + a_{j4}x^4, \quad (2)$$

where  $x = \sqrt{\epsilon_m} L / \lambda$ ,  $L$  is a characteristic particle size (for example, the sphere diameter or rod length),  $\bar{V}_j$  is the modal volume that obeys the sum rule  $\sum_j \bar{V}_j = V$ ,  $V$  is the total particle

volume,  $\eta_j$  is the eigenvalue of  $j$ -mode ( $j=1$  corresponds to the dipole eigenmode),  $a_{j2}$  and  $a_{j4}$  are MEM parameters depending on the generalized aspect ratio. Our definition of polarizability follows Bohren and Huffman's book.<sup>7</sup> It differs from Eq. (3) of Ref.<sup>20</sup> by the absence of host dielectric function in front of Eq. (18). This does not affect the resulting physical quantities as the induced dipole moments coincide in both definitions.

In Eq. (2), the first term ( $\sim x^2$ ) describes the retardation correction of polarizability (or dynamic depolarization<sup>33,34</sup>) due to finite particle size, the second term describes the radiative reaction correction ( $\sim x^3$ ),<sup>35</sup> and the last term ( $\sim x^4$ ) corresponds to an approximate high-order correction with neglecting the interactions between different electrostatic modes (cross terms). It should be noted that there is some close similarity between the MEM, quasi-static approximation (QSA)<sup>36,37</sup> and previously reported analytical approximation by Kuwata *et al.*<sup>38</sup> However, the important difference between MEM and Kuwata *et al.* approximation<sup>38</sup> is that the latter was developed as an extension of Mie theory for small spheres and then applied empirically for scattering spectra of plasmonic rods. By contrast, the MEM provides a universal description of the extinction spectra for a representative library of the NP shapes and morphologies. Besides, MEM is formulated using electrostatic eigenmode expansion accomplished by size- and shape-dependent corrections for dynamic depolarization and radiation damping.<sup>39,40</sup>

Four parameters  $\eta_j$ ,  $\bar{V}_j$ ,  $a_{j2}$ ,  $a_{j4}$  are calculated by minimizing the deviations of the MEM solution from benchmark numerical simulations. A remarkable advantage of MEM is that the fitting parameters for metal particles depend only on the generalized aspect ratio  $h \equiv AR$  and do not depend on the particle size, composition, or environment. In summary, MEM provides straightforward, accurate analytical models to simulate extinction, scattering spectra, and other electromagnetic properties of arbitrarily shaped plasmonic NPs. Owing to their analytical simplicity, MEM models can be easily implemented on any desk PC to simulate plasmonic

response from realistic experimental models involving size and shape polydisperse complicated by random orientations.

In principle, the MEM approach can also be applied to the coated particles; however, it would require multiple benchmark simulations to find MEM parameters for a particular NP coating. Fortunately, this obstacle can be avoided, and the problem can be easily solved using the previously developed dipole equivalence method (DEM). In our previous report,<sup>17</sup> we applied this approach to coated nanorods excited along the major axis. Here, we generalize the MEM+DEM method for variously shaped particles with possible random orientations.

To combine MEM with DEM, we recast first Eq. (1) as

$$\alpha_1^p = R_{1ev}^3 \sum_j q_j^p(h_1) \beta_{1j}^p, \quad (3)$$

$$\beta_{1j}^p = \frac{\varepsilon_1 - \varepsilon_m}{3\varepsilon_m + 3L_{1mj}^p(\varepsilon_1 - \varepsilon_m)}, \quad (4)$$

$$q_j^p(h_1) = \bar{V}_j^p / V_1, \quad (5)$$

where the superscript  $p$  stands for a specific polarization of the incident electric field  $\mathbf{E}_0^p$ ; the modal volume fraction  $q_j^p(h_1)$  depends on the core aspect ratio  $h_1 = AR$ . The generalized polarizability (3) is calculated as a weighted sum of the normalized modal polarizabilities (4) that have the same form as common normalized electrostatic polarizabilities<sup>17</sup> calculated with the effective modal depolarization factors  $L_{1mj}^p$ . For arbitrarily shaped particles and a specific polarization of the incident field, these factors account for retardation and radiation-damping effects in the following MEM form

$$L_{1mj}^p = \frac{1}{1 - \eta_j^p(h_1)} - A_j^p(h_1, \varepsilon_m), \quad (6)$$

$$A_j^p(h_1, \varepsilon_m) = a_{j2}^p(h_1)x_{1m}^2 + i\frac{2}{9}q_j^p(h_1)X_{1m}^3 + a_{j4}^p(h_1)x_{1m}^4, \quad (7)$$

$$x_{1m} = \frac{L_1 k_m}{2\pi}, \quad X_{1m} = R_{1ev} k_m, \quad k_m = k\sqrt{\varepsilon_m} = \frac{2\pi}{\lambda}\sqrt{\varepsilon_m}, \quad (8)$$

where  $R_{1ev}$  and  $L_1 = L$  are the equivolume sphere radius of the core and its characteristic size, respectively. The first term in Eq. (6) corresponds to the shape-dependent retardation correction, whereas the second one describes the radiation damping in terms of the shape-independent equivolume radius parameter  $X_{1m} = k_m R_{1ev}$  multiplied by the modal volume fractions. The last term in Eq. (7) accounts for small contributions  $\sim x_{1m}^4$  multiplied by shape-dependent modal coefficients  $a_{j4}(h_1)$ . If we consider the first dipole mode only ( $j=1$ ), the radiation damping term in Eq. (4) denominator reduces to well-known<sup>33-35</sup> shape-independent form  $i \frac{2}{3} X_{1m}^3$ .

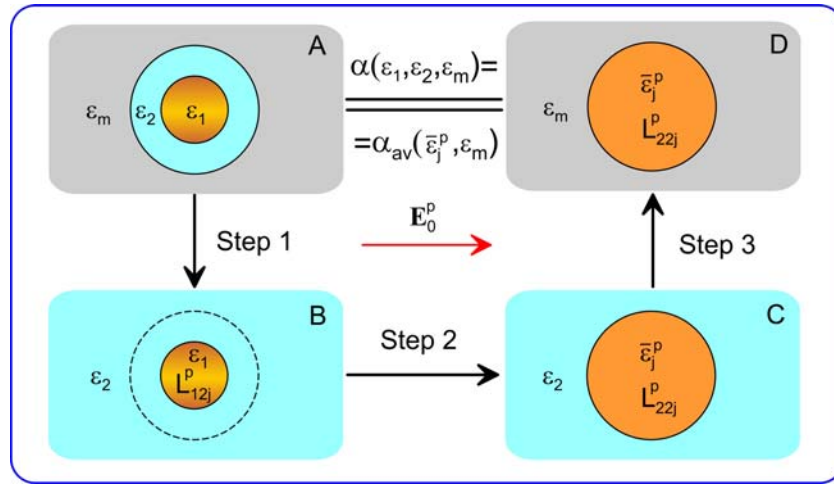


**Figure 2.** Scheme for calculating the MEM polarizability of coated plasmonic nanoparticles using DEM.

Our goal is to obtain an analytical expression for the generalized MEM polarizability of coated particles by combining MEM Eqs. (3-4) with DEM<sup>19</sup> (Figure 2). In the first step, we place the plasmonic core in a homogeneous host medium with the shell dielectric permittivity  $\epsilon_2$ . Suppose we surround the core with an imaginary surface coinciding with the shell of the original two-layer particle (dashed line in panel B). In that case, the core polarizability will not change. In the second step, we replace the imaginary particle with an averaged particle with equivalent MEM polarizability (panel C). By equating both polarizabilities, we arrive at the following DEM equation



$$R_{1ev}^3 \sum_j q_{1j}^p \frac{\varepsilon_1 - \varepsilon_2}{\varepsilon_2 + L_{12j}^p (\varepsilon_1 - \varepsilon_2)} = R_{2ev}^3 \sum_j q_{2j}^p \frac{\bar{\varepsilon}_j^p - \varepsilon_2}{\varepsilon_2 + L_{22j}^p (\bar{\varepsilon}_j^p - \varepsilon_2)}. \quad (9)$$

Unfortunately, Eq. (9) cannot be resolved with respect to  $\bar{\varepsilon}_j^p$ . To avoid this difficulty, we

propose the following modal extension of DEM: we apply Eq. (9) to each mode  $j$  separately.

The validity of this assumption will be shown below when compared with rigorous calculations of cross sections. For independent modes, Eq. (9) gives the following simple solution

$$\bar{\varepsilon}_j^p = \varepsilon_2 \left( 1 + \frac{B_{12j}^p}{1 - L_{22j}^p B_{12j}^p} \right), \quad (10)$$

$$B_{12j}^p = f_{12} \frac{q_j^p(h_1)}{q_j^p(h_2)} \frac{\varepsilon_1 - \varepsilon_2}{\varepsilon_2 + L_{12j}^p (\varepsilon_1 - \varepsilon_2)}, \quad (11)$$

where  $f_{12} = (R_{1ev} / R_{2ev})^3$  is the core volume fraction. Explicit expressions for effective depolarization factors and related quantities are as follows:

$$L_{i2j}^p = \frac{1}{1 - \eta_j^p(h_i)} - A_j^p(h_i, \varepsilon_2), \quad i = 1, 2, \quad (12)$$

$$A_j^p(h_i, \varepsilon_2) = a_{j2}^p(h_i) x_{i2}^2 + i \frac{2}{9} q_j^p(h_i) X_{i2}^3 + a_{j4}^p(h_i) x_{i2}^4, \quad i = 1, 2, \quad (13)$$

$$x_{i2} = \frac{L_i k_2}{2\pi}, \quad X_{i2} = R_{iev} k_2, \quad i = 1, 2, \quad (14)$$

where  $k_2 = k\sqrt{\varepsilon_2} = (2\pi/\lambda)(\sqrt{\varepsilon_2})$ ,  $L_1$  and  $L_2$  are the characteristic sizes of core and shell, respectively; the modal volume fractions  $q_j^p(h_i)$  depend on the aspect ratio of core ( $h_1$ ) and shell ( $h_2$ ), respectively.

In the third step, we place the averaged particle in panel C in the host medium  $\varepsilon_m$  (panel D) to calculate the averaged polarizability

$$\alpha_{av}^p = R_{2ev}^3 \sum_j q_{2j}^p \frac{\bar{\varepsilon}_j^p - \varepsilon_m}{3\varepsilon_m + 3L_{2mj}^p (\bar{\varepsilon}_j^p - \varepsilon_m)}, \quad (15)$$

$$L_{2mj}^p = \frac{1}{1 - \eta_j^p(h_2)} - A_j^p(h_2, \varepsilon_m), \quad (16)$$

$$A_j^p(h_2, \varepsilon_m) = a_{j2}^p(h_2) x_{2m}^2 + i \frac{2}{9} q_j^p(h_2) X_{2m}^3 + a_{j4}^p(h_2) x_{2m}^4, \quad (17)$$

$$x_{2m} = \frac{L_2 k_m}{2\pi}, \quad X_{2m} = R_{2ev} k_m, \quad k_m = k\sqrt{\varepsilon_m}. \quad (18)$$

By comparing physical pictures in panels A and D, we conclude that Eq. (15) gives the desired expression for the MEM polarizability of coated particles. Remarkably, Eq. (15) includes the core parameters MEM only, while the coating is described by its external size, shell thickness, and dielectric function, and these shell quantities are used with the same MEM functions of the core.

The above MEM+DEM scheme can easily be generalized for an arbitrary multilayered coating by recursive application of MEM to the coated averaged particle in panel D. A simplest case of a plasmonic nanorod with two-layered coating has been considered in our previous work.<sup>17</sup>

The averaged over random particle orientations cross sections read<sup>23</sup>

$$\langle C_{ext} \rangle = \pi R_2^2 \langle Q_{ext} \rangle = 4\pi \frac{1}{k'_m} \text{Im} \left( k_m^2 \frac{\alpha_{av}^x + \alpha_{av}^y + \alpha_{av}^z}{3} \right), \quad (19)$$

$$\langle C_{sca} \rangle = \pi R_2^2 \langle Q_{sca} \rangle = \frac{8}{3} |k'_m|^4 \frac{|\alpha_{av}^x|^2 + |\alpha_{av}^y|^2 + |\alpha_{av}^z|^2}{3}, \quad (20)$$

where the angular brackets designate orientation averaging,  $k'_m = \text{Re}(k_m) = (2\pi / \lambda) \text{Re}(n_m)$ , and superscripts  $x, y, z$  stand for polarizations of the incident light along the corresponding frame axes related to the particle. Equations (19-20) are applicable for an arbitrary absorbing host and for a dielectric environment, they reduce to known results.<sup>26</sup>

## 4. Results and discussion.

### 4.1. Gold and silver nanorods

Before calculating the extinction and scattering spectra of coated particles, we performed several accuracy tests by comparing the extinction and scattering spectra obtained with COMSOL and TMM codes for metal nanorods. In all simulations, the particle diameter was 15 nm, typical for most experimental samples used in various applications.<sup>41</sup> Figure S5 demonstrates excellent agreement between both methods for a most challenging test with long nanorods ( $AR = 6$ ). Similarly, excellent agreement was obtained for other particle models. Finally, we performed

extensive simulations for AuNRs with fixed and random orientations using MEM codes in comparison with benchmark TMM calculations (Figure S6). MEM parameters for AuNRs were taken from Ref.<sup>20</sup> and are listed in SI. We found excellent agreement between the major extinction and scattering plasmonic peaks at longitudinal excitation and small differences for a minor perpendicular peak.

Figure 3 shows the extinction spectra of randomly oriented gold nanorods with a diameter of 15 nm, aspect ratios from 2 to 6, and the shell thicknesses of 0, 3, and 30 nm. From a practical point of view, the region of the main spectral peak associated with the longitudinal dipole resonance is of the most significant interest. With an increase in the coating thickness, the extinction peak moves to the red<sup>42,43</sup> and is strongly (for short nanorods) or slightly (for longer ones) increased in the peak amplitude.

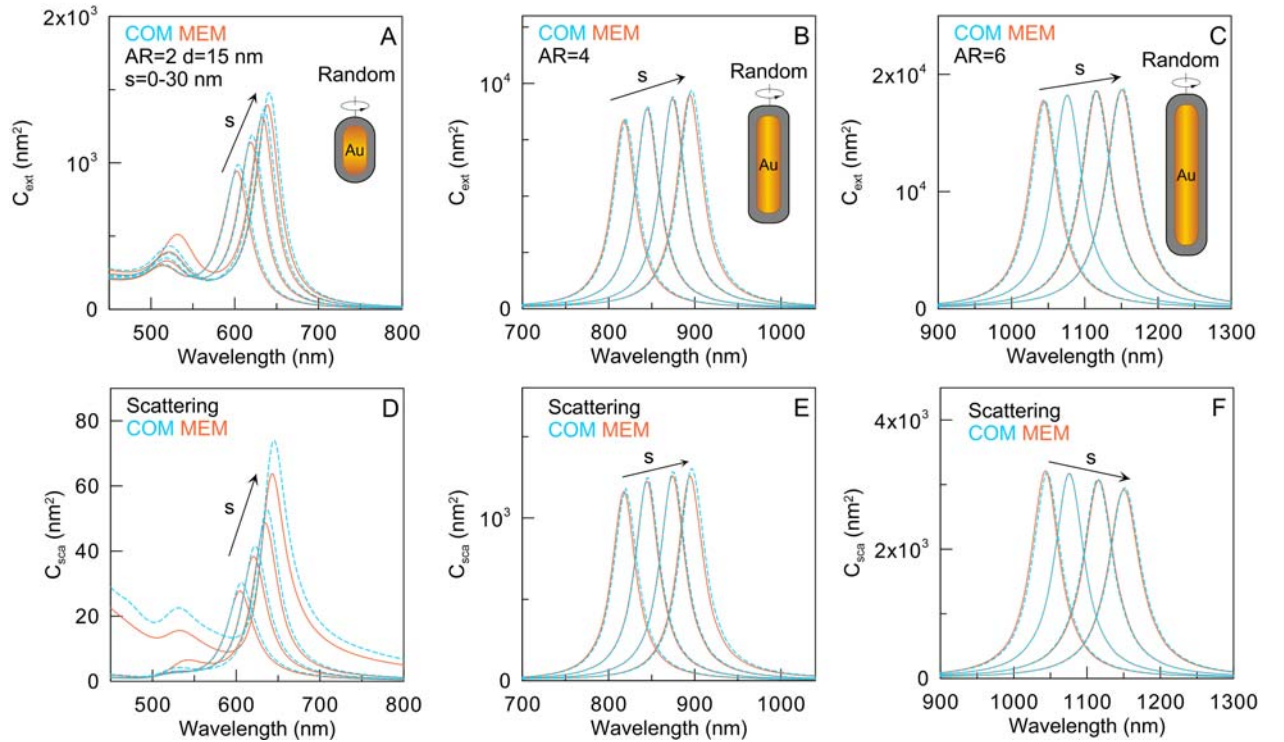


**Figure 3.** Extinction (A-C) and scattering (D-F) spectra of randomly oriented Au bare and coated randomly oriented nanorods were calculated using COM (blue) and MEM (red). The particle diameter is 15 nm, and their aspect ratio is 2 (A, B), 4 (B, E), and 6 (C, D). The coating thicknesses are 0, 3, 10, and 30 nm; the coating refractive index is 1.5.

Interestingly, for long rods, the scattering peak does not increase but decreases with increasing thickness of the coating (panel F). Also, for small AuNRs, an increase in the shell thickness from 3 to 30 nm strongly increases the short-wavelength scattering (panel D).

Extinction and scattering MEM spectra of randomly oriented silver nanorods reproduce the main longitudinal plasmonic TMM peak quite accurately (Figure S7). In contrast to data for gold nanorods, the short wavelength portion of extinction and scattering spectra demonstrates a complicated structure. MEM reproduces two minor peaks near 355 and 375 nm with acceptable accuracy. In addition, spectra in Figure S7 exhibit multipole resonances that MEM cannot reproduce.

The physical origin of multipole peaks is elucidated by Figure 4, where panels A and B show extinction and scattering spectra for a randomly oriented ensemble of AgNRs with  $AR = 4$ , whereas panels C and D show similar spectra for two specific fixed orientations. A 475-nm peak in panel A is related to quadrupole<sup>44</sup> absorption because it is absent in scattering spectra (panel B). This quadrupole resonance is excited most strongly by TM plane wave (electric field lies in  $(\mathbf{a}, \mathbf{k})$  plane;  $\mathbf{a}$  is the rod symmetry axis) whose wave vector is directed at 54 degrees with respect to the symmetry axis  $\mathbf{a}$  (dashed spectrum in panel C). It should be emphasized that the 475-nm quadrupole peak disappears at longitudinal excitation due to symmetry constraints. Similarly to the scattering spectrum for random ensemble (panel B), this peak is not seen in scattering spectrum in panel D.

The second multipole peak in panel A is located near 410 nm, which is also caused by absorption rather than scattering. However, in contrast to the 475-nm quadrupole, this 410-nm peak is most effectively excited by the longitudinal electric field (solid blue line in panel C). Although we observe a small similar scattering peak in panel D, its contribution is negligible compared to the absorption.

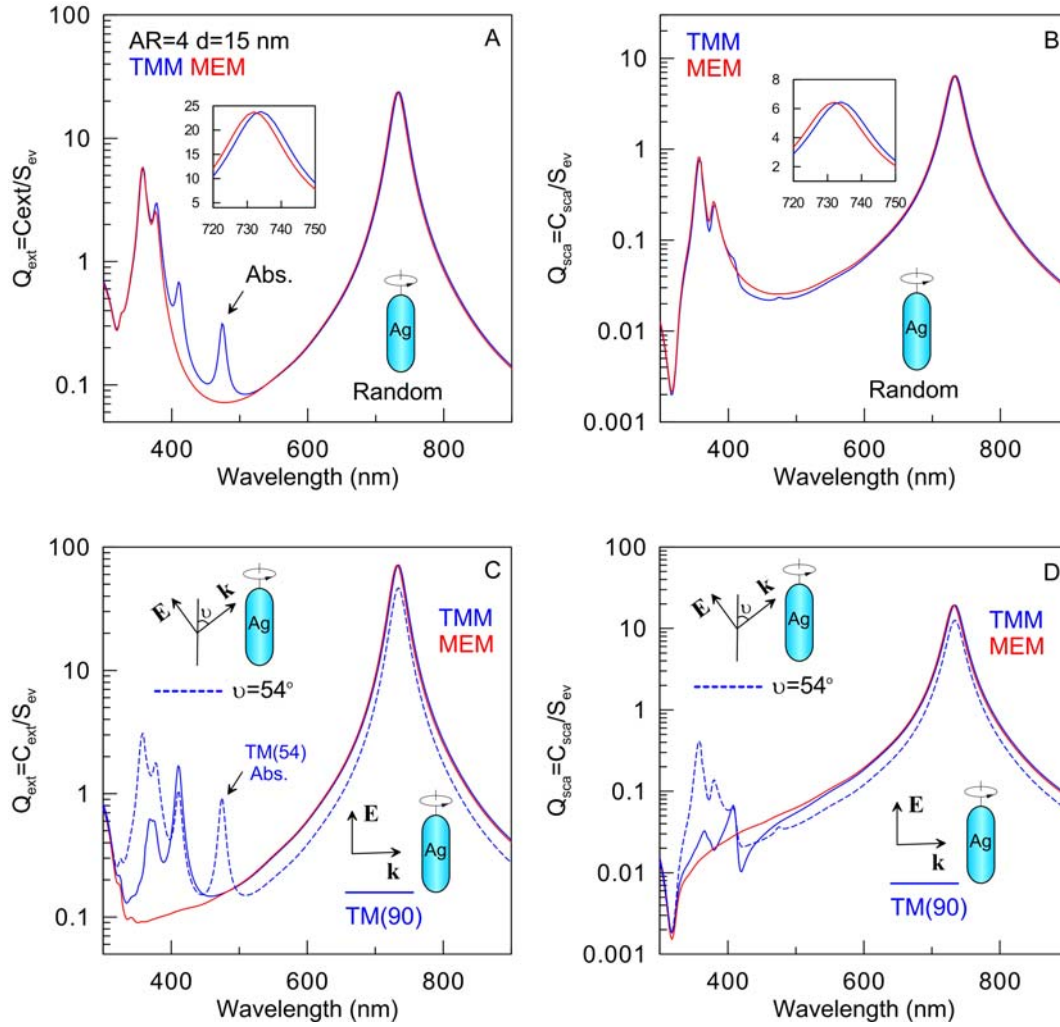


**Figure 4.** Extinction and scattering spectra calculated by the T-matrix method (TMM, blue) and MEM (red) for random particle orientations (A, B) and excitation by TM incident wave with wave vector directed perpendicularly (solid blue line) and at 54 degrees (dashed blue line) to the rod symmetry axis (C, D). The arrow in panel C indicates the quadrupole absorption peak. Note that there is excellent agreement between TMM and MEM in the description of the main plasmonic peak (solid blue and red curves).

Figure 5 illustrates the quality of MEM approximation in describing the main plasmonic peaks of coated silver nanorods. Some blue deviation of MEM spectra is observed for a minimal aspect ratio  $AR=2$ , while the agreement becomes almost perfect for longer nanorods. We emphasize that we used the same universal MEM parameters as those for gold particles in this case. If one makes an independent MEM fitting for silver nanorods, the quality of modeling the

spectra of coated particles will be higher. As for long AuNRs, panels E and F demonstrate an unexpected decrease in scattering amplitude for coated silver nanorods.

In most sensing, imaging, and other biological and medical applications, the maximal sizes of silver and gold nanorods are less than  $20 \times 120$  nm. Therefore, we conclude that a simple MEM+DEM approach can be used to simulate the plasmonic properties of dielectric-coated nanorods with reasonable accuracy.

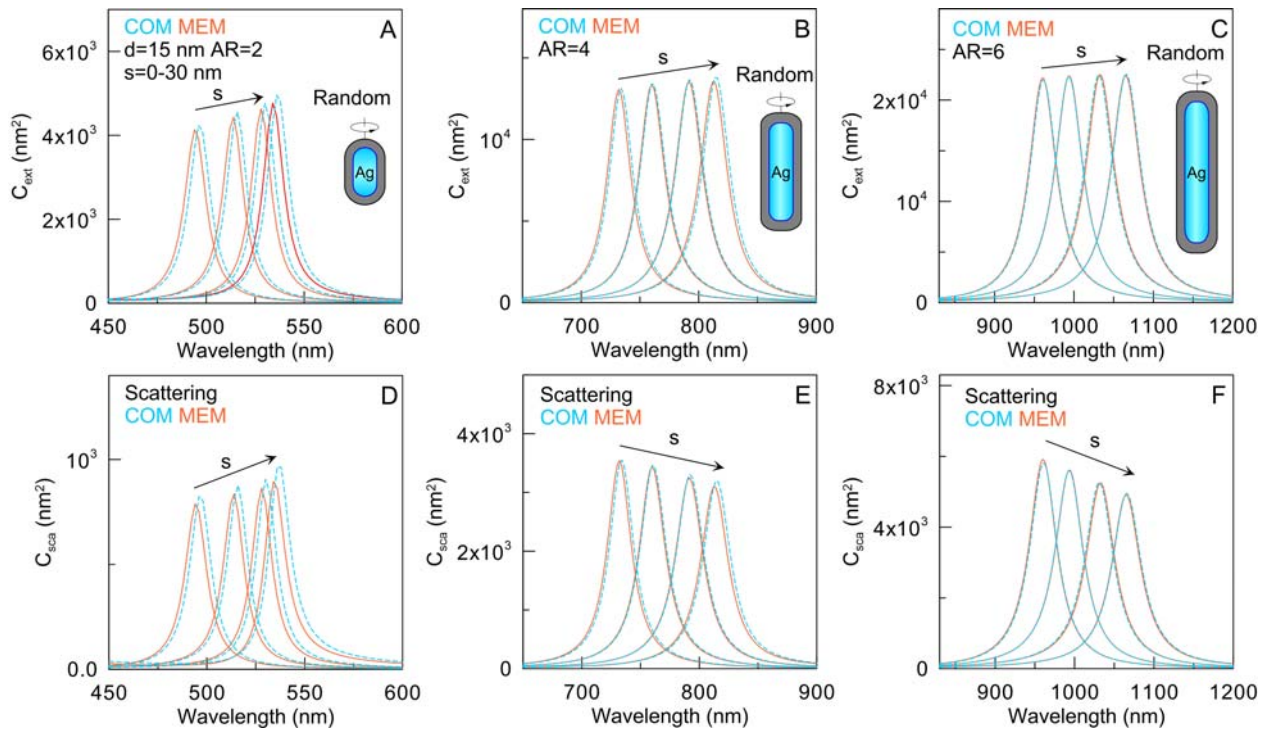


**Figure 5.** Extinction (A-C) and scattering (D-F) spectra of randomly oriented Au bare and coated randomly oriented nanorods were calculated using COM (blue) and MEM (red). The particle diameter is 15 nm, and their aspect ratio is 20 (A), 4 (B), and 6 (C). The coating thickness is 0, 3, 10 (B, C), and 30 nm; the coating refractive index is 1.5. Note decreased scattering peaks with increased shell thickness (panels E and F).

#### 4.2. Gold and silver nanodisks

To verify the accuracy of MEM for disks, we compared benchmark T-matrix (TMM) spectra with those calculated by MEM. Figure S8 illustrates excellent agreement between TMM and MEM extinction and scattering spectra for thin bare Au disks with 10 and 20 nm thicknesses. At the same time, some minor differences are observed for thicker 30-nm disks.

Similarly, for coated gold nanodisks, we observed excellent agreement between MEM and COMSOL extinction and scattering spectra of thin 10-nm (data not shown) and good agreement for 20-nm particles with the coating thickness ranging from 3 to 30 nm (Figure 6 A,B).

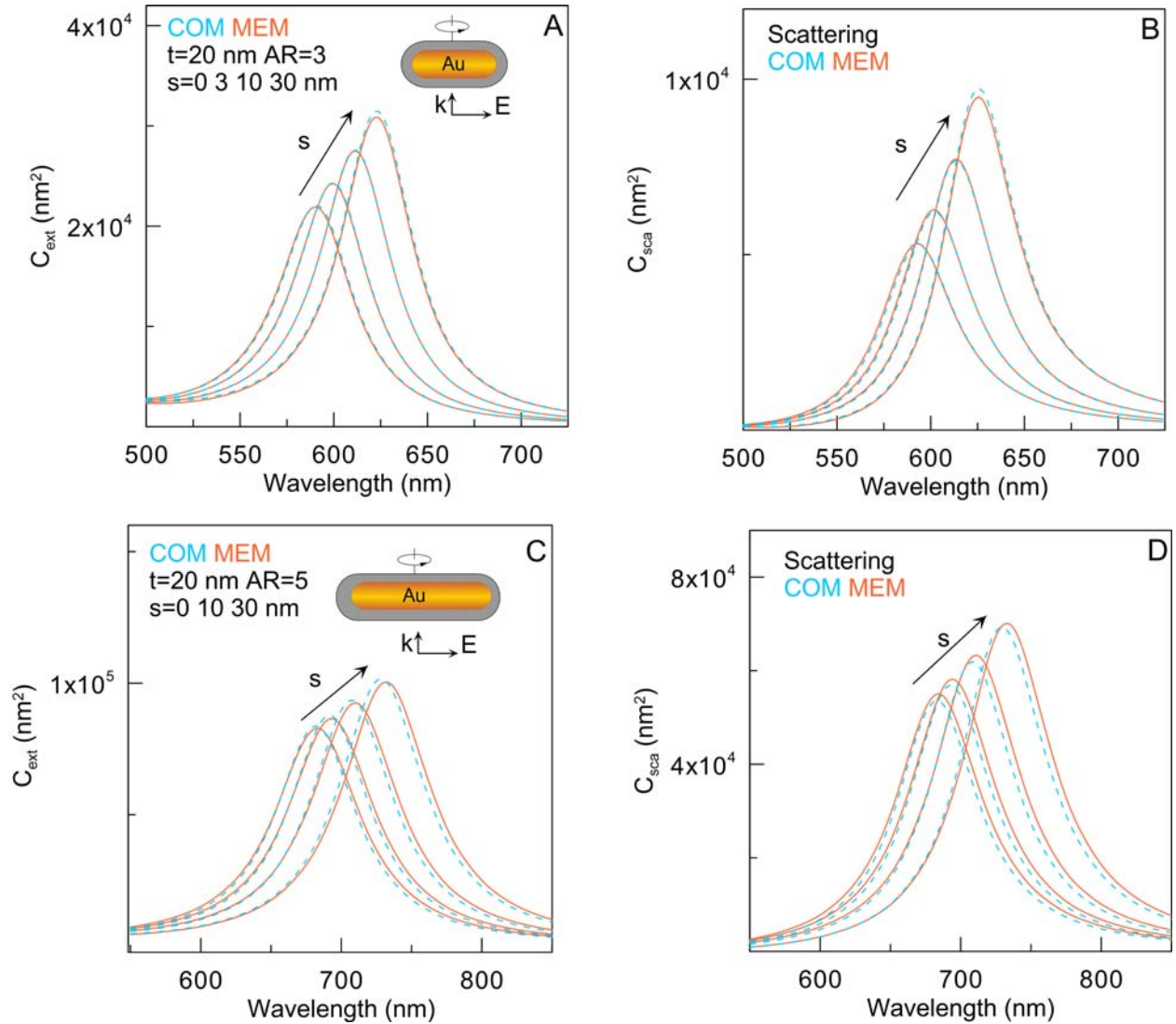


**Figure 6.** Extinction (A, C) and scattering (B, D) spectra of gold bare and coated nanodisks were calculated using MEM (red lines) and COMSOL (blue dashed lines). The particle thickness is  $L = 20$  nm, and their aspect ratios are 3 (A, B) and 5 (C, D). The coating thickness varies from 0 to 30 nm; the coating refractive index is 1.5. The wave vector is directed along the disk axis. However, the MEM approximation accuracy becomes lower with increased gold disk thickness and diameter (Figure 6 C, D). In particular, Figure 7A shows an evident red shift and broadening of MEM spectra compared to COM ones when calculated for both bare (solid lines) disks and coated (dashed lines) nanodisks with 30-nm thickness. A possible physical origin behind the low

accuracy of MEM could be attributed to the limited size-dependent ( $\sim x^4$ ) correction for such large disks. Such limitations become quite evident if we consider the case when both the wave vector and electric field are perpendicular to the disk symmetry axis (Figure 7B). Specifically, panel B clearly demonstrates strong excitation of the quadrupole absorption mode near 650 nm, making a dominant contribution to the extinction spectrum (black line). Note that for randomly oriented disks, this quadrupole peak is not seen (green spectrum).

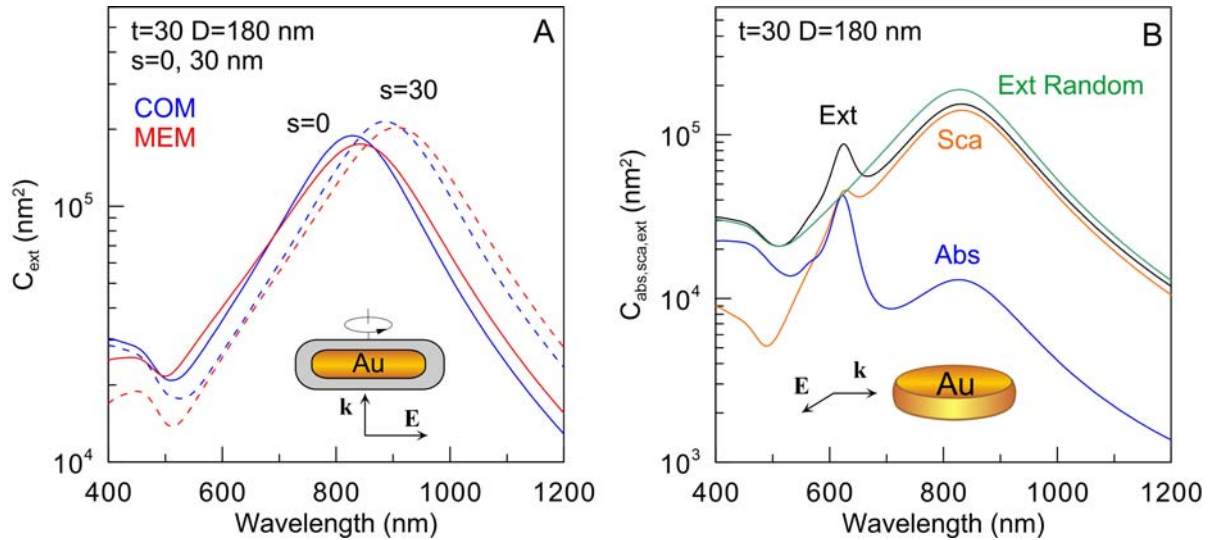


**Figure 7.** (A) Extinction spectra calculated by COMSOL (blue) and MEM (red) for bare (solid lines) and coated (dashed lines,  $s = 30$  nm) nanodisks; the incident wave vector is parallel to the symmetry axis. (B) Absorption (blue), scattering (orange), and extinction (black) spectra for perpendicular incidence. The green spectrum corresponds to random particle orientations.

Thus, the MEM approximation can be used to simulate the extinction and scattering spectra of oblate gold particles if their diameter does not exceed 150 nm and the coating thickness is less than 20-30 nm, depending on the disk diameter.

To verify the accuracy of COMSOL data for silver disks, we compared benchmark T-matrix (TMM) spectra with those calculated by COMSOL. Figures S9 and S10 illustrate almost perfect agreement between TMM and COMSOL spectra for 20-nm and 30-nm silver disks with aspect ratios from 3 to 6. Some minor differences are observed only for the short-wavelength multipole peaks for the largest 30x180 nm disks (Figures S10 C, D).



Figure 8 shows extinction and scattering spectra for 20-nm silver disks at in-plane excitation. Similar to the data in Figure 6, we observe excellent agreement between MEM and COMSOL spectra when the disk diameter is less than 60 nm. For larger disks with diameters of 100 nm (the aspect ratio is 5), we note more evident deviations of MEM spectra from COMSOL ones. Similar data are presented in the ESI file for thin 10-nm and thick 30-nm disks (Figure S11).

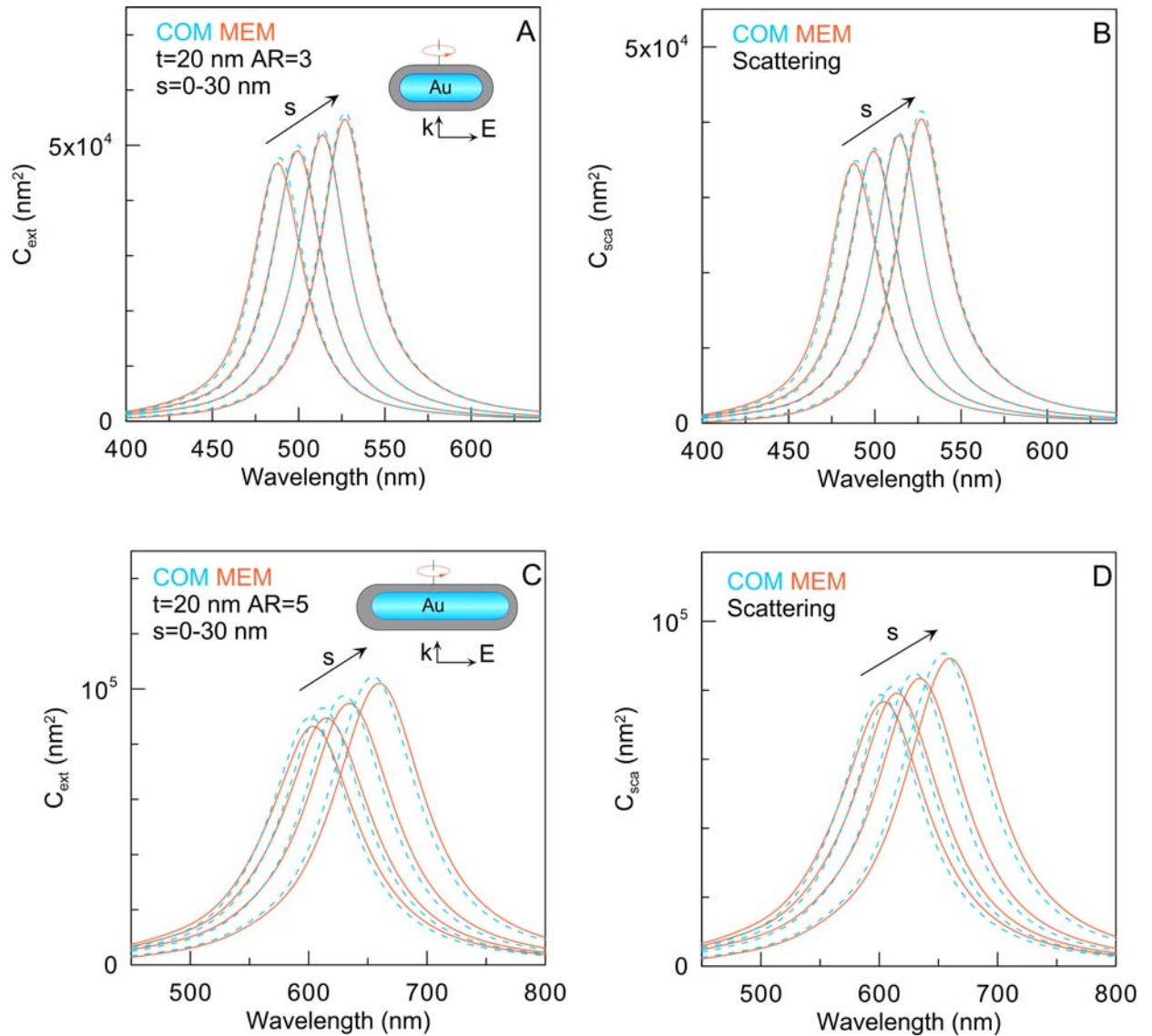


**Figure 8.** Extinction (A, C) and scattering (B, D) spectra of silver bare and coated nanodisks were calculated using MEM (red lines) and COMSOL (blue dashed lines). The particle thickness is  $L = 20$  nm, and their aspect ratios are 3 (A, B) and 5 (C, D). The coating thickness varies from 0 to 30 nm; the coating refractive index is 1.5. The wave vector is directed along the disk axis.

In summary, the MEM approximation can be used to simulate the extinction and scattering spectra of silver disk-shaped particles if their thickness and diameter do not exceed 20 and 100 nm and the coating thickness is less than 30 nm, depending on the disk diameter.

### 4.3. Gold and silver nanoprisms

Figures S12-S13 compare COM and MRM extinction and scattering spectra for thin Au nanoprisms with thicknesses ranging from 10 to 20 nm and aspect ratios ranging from 3 to 15. Note that MEM does not reproduce multipole peaks but approximates major plasmonic peaks well. We derived new MEM parameters for MEM calculations that ensure good accuracy within much broader size and shape ranges compared to those in Ref.<sup>20</sup>. Similar conclusions can also be drawn for silver nanoprisms (Figure S14). Our nanoprism model has the same smooth edges with a small rounding radius as proposed in Ref.<sup>20</sup>. Effects of larger rounding radii have been reported in Ref.<sup>45</sup>

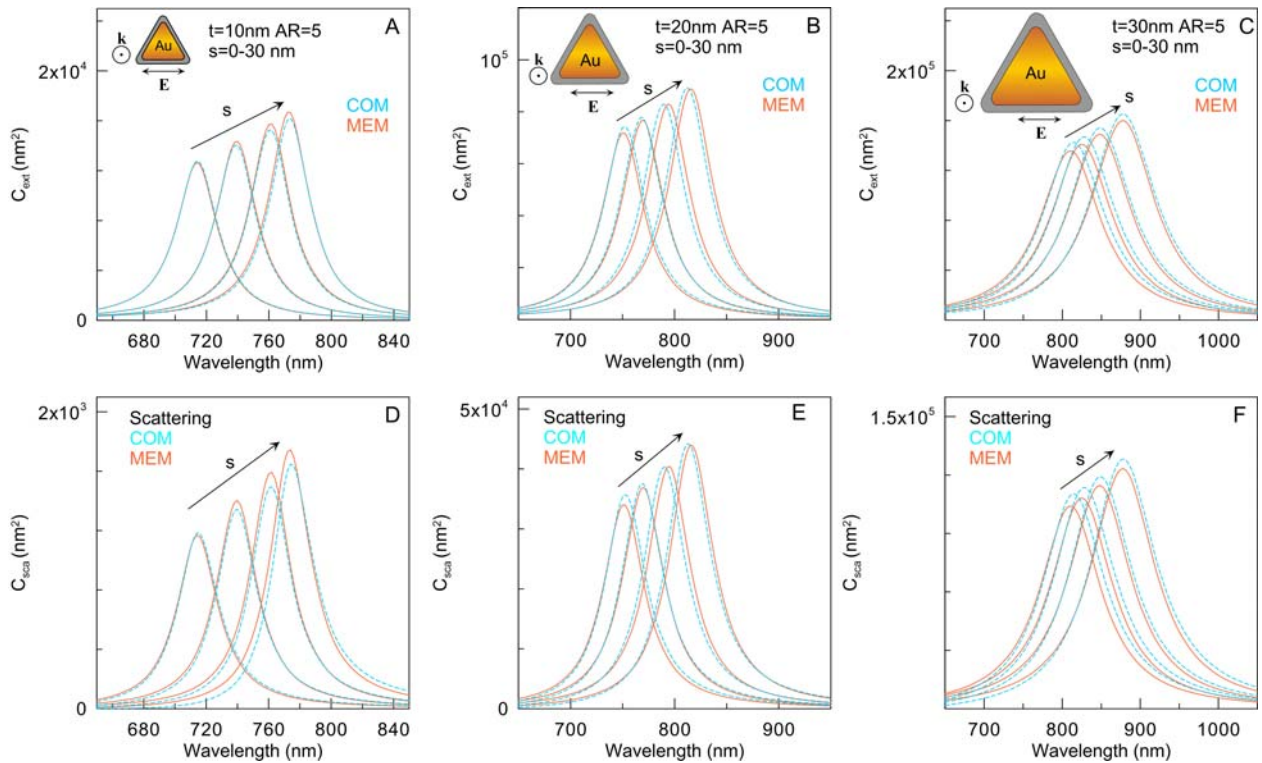


**Figure 9.** Extinction (A–D) and scattering (E–F) spectra of gold bare and coated nanoprisms were calculated using MEM (orange) and COMSOL (blue). The prism thickness  $t = 10$  (A, E),

20 (B, F), and 30 nm (D, G); the core aspect ratio  $AR = L/t$  is constant and equals 5, and the coating thicknesses  $s$  are 0, 3, 10, and 30 nm. The wave vector is directed along the nanoprism side (in-plane excitation).

Figure 9 illustrates the effects of coating on the extinction and scattering plasmonic peak position and amplitude as predicted by COMSOL and MEM. These simulations show that MEM approximation gives good accuracy provided that the prism sizes are within  $30 \times 150$  nm and the coating thickness is less than 30 nm. These limits satisfy typical parameters of gold nanotriangles fabricated by modern chemical protocols.<sup>46</sup> The same conclusion applies to coated silver nanoprisms (Figure 10).

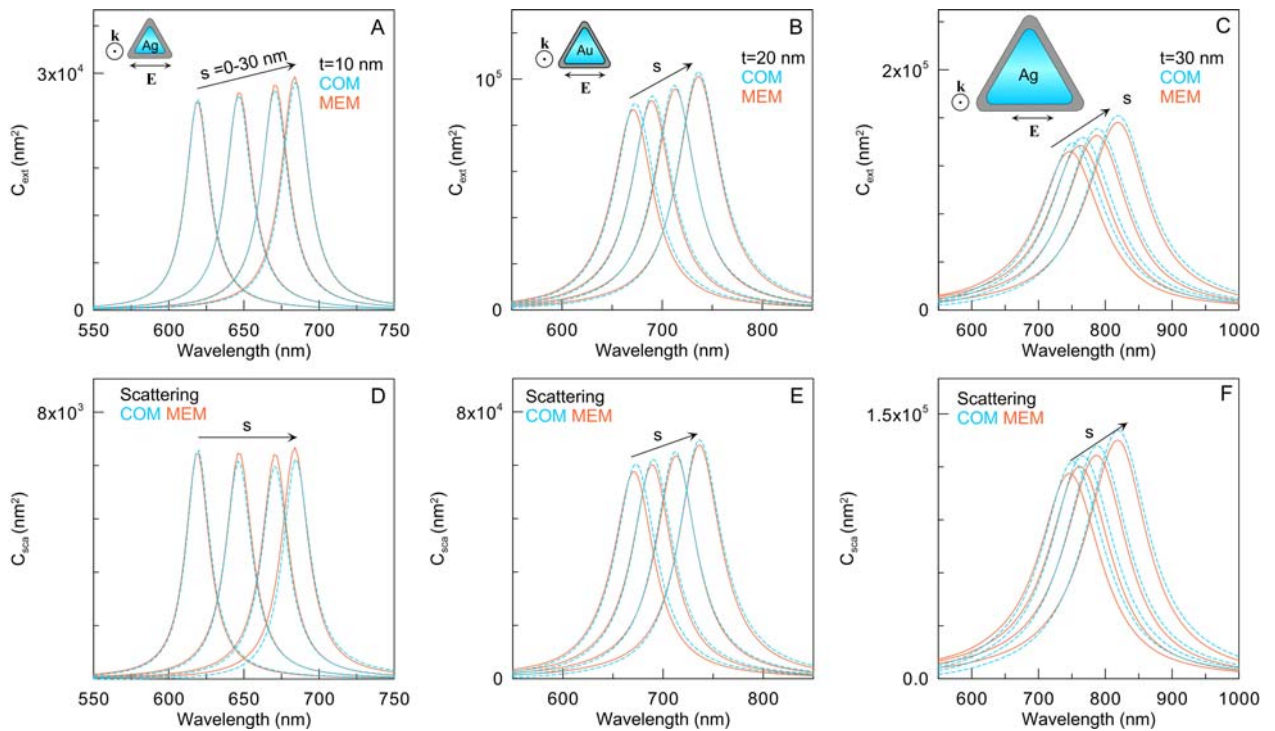


**Figure 10.** Extinction (A–C) and scattering (D–F) spectra of silver bare and coated nanoprisms were calculated using MEM (orange) and COMSOL (blue). The prism thickness  $t = 10$  (A, D), 20 (B, E), and 30 nm (C, F); the core aspect ratio  $AR = L/t$  is constant and equals to 5, and the coating thicknesses  $s$  are 0, 3, 10, and 30 nm. The wave vector is directed along the nanoprism side (in-plane excitation).

### 4.3. Gold bicones and bipyramids

Pentagonal gold bipyramids (BPs) are a new class of popular anisotropic nanoparticles whose extinction and scattering spectra resemble those of gold nanorods.<sup>47-48,49,50</sup> During the chemical etching of as-prepared initial AuBPs, their shape subsequently transforms to rounded BPs, then to rounded bicones (BCs), and finally to nanospheres.<sup>51</sup> Keeping in mind these intermediate shapes, we include AuBCs in our consideration.

In line with the previous report,<sup>20</sup> our analytical MEM model accurately describes the numerical LPR peaks for gold bicones (Figure S15). We showed above that for rods, disks, and nanoprisms, the analytical method MEM+DEM well describes the extinction and scattering spectra of coated particles. However, we found noticeable discrepancies in the plasmon resonance shifts predicted by the analytical method and COMSOL numerical calculations for coated bicones (Figure S16). Analytical theory for bilayer gold and silver nanospheres<sup>52</sup> predicts a linear relationship between the plasmon resonance shift and the volume fraction of the dielectric shell  $g = V_{shell} / (V_{core} + V_{shell})$ . Following this prediction, in Figure 11, we show the dependence of the plasmon extinction shift on the shell volume fraction, calculated for bicones with aspect ratios 2 and 4. It can be seen that the analytical orange curves (MEM) are very different from the numerical calculation data (black crosses). The physical reasons for this discrepancy can be associated with a strong field inhomogeneity inside and around the particle (Figure 12). This contradicts the principle of dipole equivalence based on the equality of dipole moments and polarizabilities of multilayer and a homogeneous equivalent particle. Physically, such equivalence implicitly assumes a uniform field distribution in the equivalent particle, which is violated in the case of bicones, for which the vertices are singular points of strong field concentration.

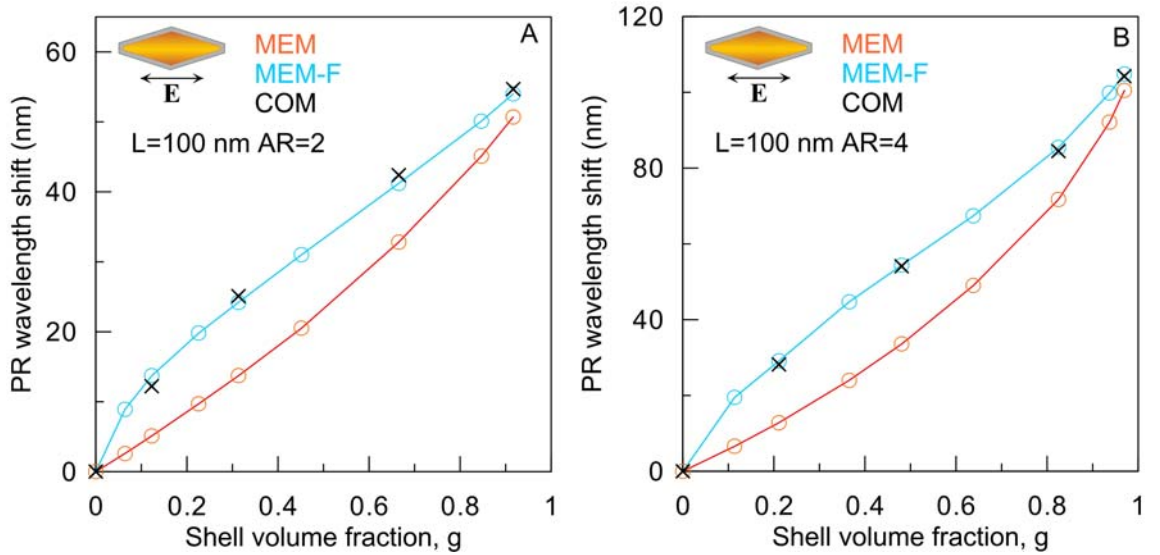


**Figure 11.** Dependences the plasmon resonance shift on the shell volume fraction  $g$  calculated by MEM (orange curve) and COMSOL (black crosses) for bicones with the total length  $L = 100$  nm and aspect ratio  $AR = 2$  (A) and 4 (B). Blue lines show calculations by the improved version of MEM-F.

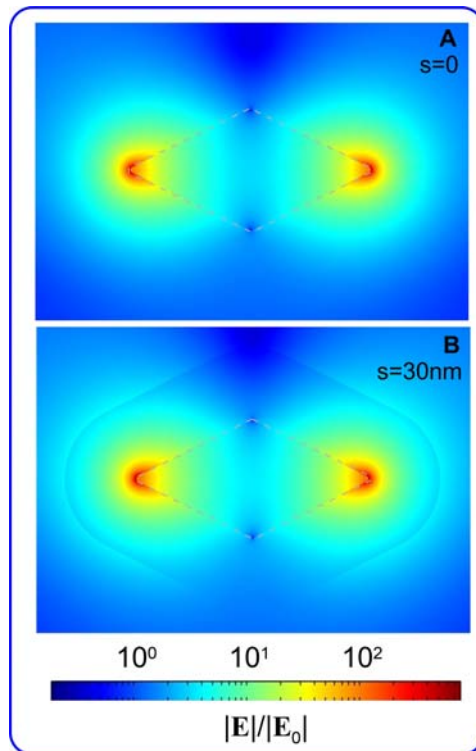


**Figure 12.** Field distribution for bare (A;  $s=0$ ) and coated (B,  $s=30$  nm) gold bicones at the longitudinal excitation along the symmetry axis. The wavelengths correspond to the major plasmonic peaks.

To eliminate this drawback of MEM, we assumed that the MEM parameters  $\eta_1$  and  $V_1$  in equation (1) can be represented in a factorized form (for simplicity, we consider below only the first mode)

$$\eta_1 = \eta_1(AR_i)f_\eta(s), V_1 = V_1(AR_i)f_V(s), \quad (21)$$

where the first factors correspond to the MEM parameters calculated for the aspect ratio of the core ( $AR_1$ ) or shell ( $AR_2$ ) according to the formulas specified in the ESI. The second factor in equation (21) considers the specific shell effects and satisfies the apparent conditions  $f_\eta(0) = 1$   $f_V(0) = 1$ . Explicit formulas for functions  $f_\eta(s)$  and  $f_V(s)$  are given in the supporting information file. We emphasize that the factorized correction (21) for the shell effect is universal and does not depend on the particle size, shape, and metal composition. Otherwise, the analytical description would be reduced to a non-universal fitting of the spectra for a specific particle shape and a specific shell thickness.

The blue curves in Figure 11 were calculated using the described scheme (called factorized MEM or MEM-F here). We see excellent agreement between the LPR shift values from analytical theory and numerical calculations. Similarly, the analytical extinction and scattering spectra (Figure 13) reproduce COMSOL in peak positions and amplitudes. One important note is in order here. Due to the strong localization of the local field near bicone tips, we observe extraordinary sensitivity of the LPR peak positions to the local dielectric environment. In particular, even for the smallest shell thickness of 1 nm, we observed the LPR shift to about 30 nm for AR=4. By contrast, the LPR shift is one order lower for spherical particles with similar shell volume fraction, less than 3 nm.<sup>52</sup> We also note different coating effects on the scattering cross section for small (panel E) and large (panel H) bipyramids at a constant bicone length.

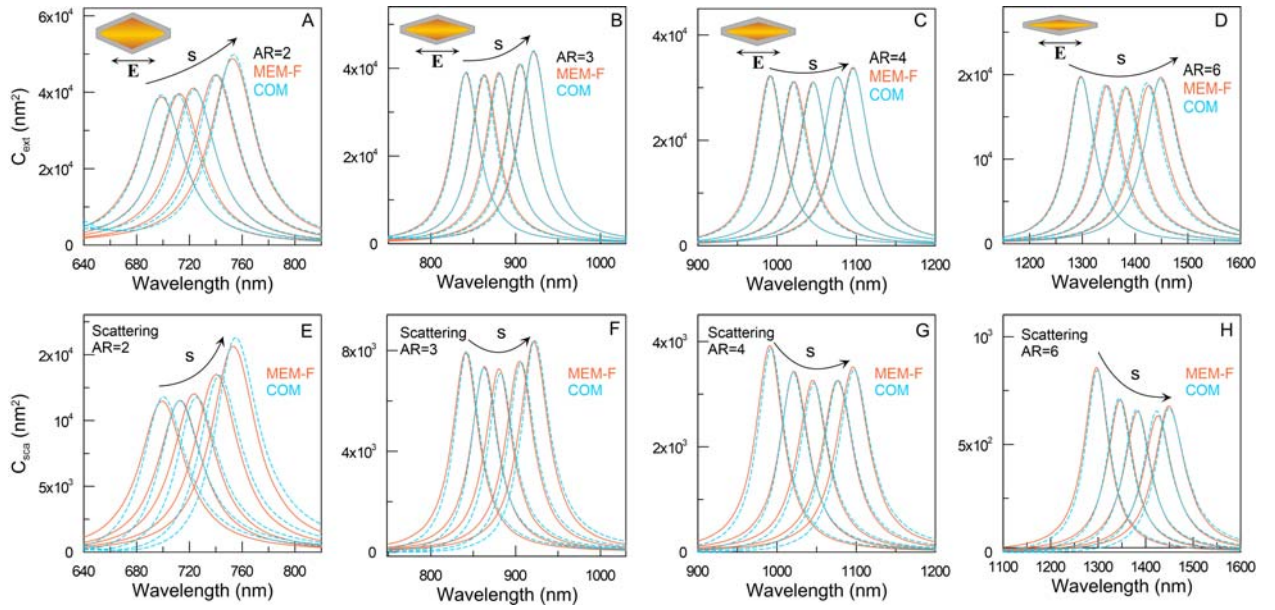


**Figure 13.** Extinction (A-D) and scattering (E-H) spectra were calculated by MEM-F (orange) and COMSOL (blue) for coated Au bicones with a total length of 100 nm and aspect ratios 2, 3, 4, and 6. The shell thicknesses are 0, 1, 3, 10, and 30 nm.

Now we proceed to the coated bipyramids. In the original MEM papers by Yu et al.<sup>20</sup>, the rounding radii of the BP tip and base were too small and did not match experimental particles. From experimental and geometrical inversion data published by Montaña-Priede et al.<sup>51</sup>, the tip rounding radius increases with a decreased rounded BP length. Similarly, the base rounding radius also increases during the chemical etching. In this work, we included both rounding effects in our geometrical BP model (for details, see the SI file, Section S1.5). Note that in the cited work<sup>51</sup>, the authors disregarded the base rounding of their BPs. It follows from the above-cited papers that the average BP width  $w \equiv d$  ranges from 20 to 35 nm, and the maximal aspect ratio  $AR = L/d$  is typically less than 6. The readers are referred to the SI file for all analytical derivations concerning the rounded BC and BP shapes and volumes. Here, we note only one key point. The initial (non-rounded) and rounded volumes of coated particles can be calculated analytically for bicone shape. The BP shape is characterized by a circle's diameter embedded in the pentagonal base and the total length of the embedded bicone. An analytical calculation of the rounded BP volume is not trivial, especially for the coated particles. To avoid this difficulty, we assumed that the volume of a coated rounded BP can be approximated as follows:

$$V_{\text{BPr}}(s) = V_{\text{BPr}}(s=0) \frac{V_{\text{BCr}}(s)}{V_{\text{BCr}}(s=0)}, \quad (22)$$

where the symbol 'r' stands for rounded particle shape. Direct numerical calculations showed excellent accuracy of the above approximation (22) with relative errors less than 0.002%.

Figure 14 shows the extinction and scattering spectra of coated BPs for three aspect ratios that ensure the LPR peak positions within the most important biological window, 650-900 nm. After dielectric coating with a thickness of 1 to 30 nm, the LPR positions shift to the red by 70 nm at AR=3 and 100 nm at AR =5. One can see excellent accuracy of the MEM+DEM approximation without any factorization, which we had to apply for more sharp bicones. Additional spectra can be found in the SI file.

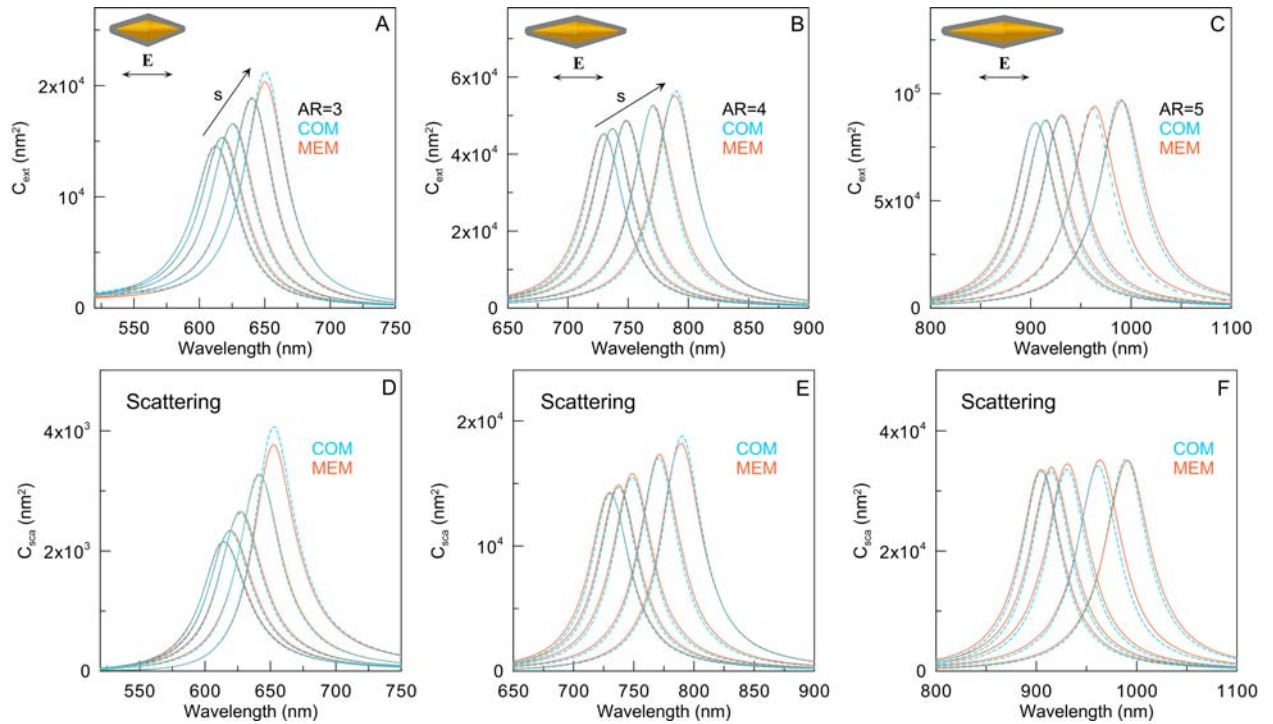


**Figure 14.** Extinction (A-C) and scattering (D-F) spectra were calculated by MEM (orange) and COMSOL (blue) for coated rounded gold bipyramids with a constant width of 30 nm and aspect ratios 3, 4, and 5. The shell thicknesses are 0, 1, 3, 10, and 30 nm.

In contrast to gold BPs, silver pentagonal BPs are rare examples in the plasmonic nanoparticle family.<sup>53</sup> Nevertheless, several works reported synthesizing and characterizing anisotropic silver nanoparticles similar to gold BPs, mainly silver right bipyramids.<sup>54-56</sup> Figure



15 illustrates an application of the MEM+DEM method to the coated silver pentagonal BPs. Because of sufficiently large rounding radii, there was no need for additional factorization to reproduce COMSOL-simulated extinction and scattering spectra. The only difference from the AuBP case is that we modified MEM parameters slightly (see SI file, Section 1.5). Let us note a change in the tendency in the scattering teaks from increasing to decreasing with increasing thickness of the coating of short (E) and long (H) bipyramids. Clearly, the amplitudes of absorption peaks increase in all cases with increasing coating thickness.

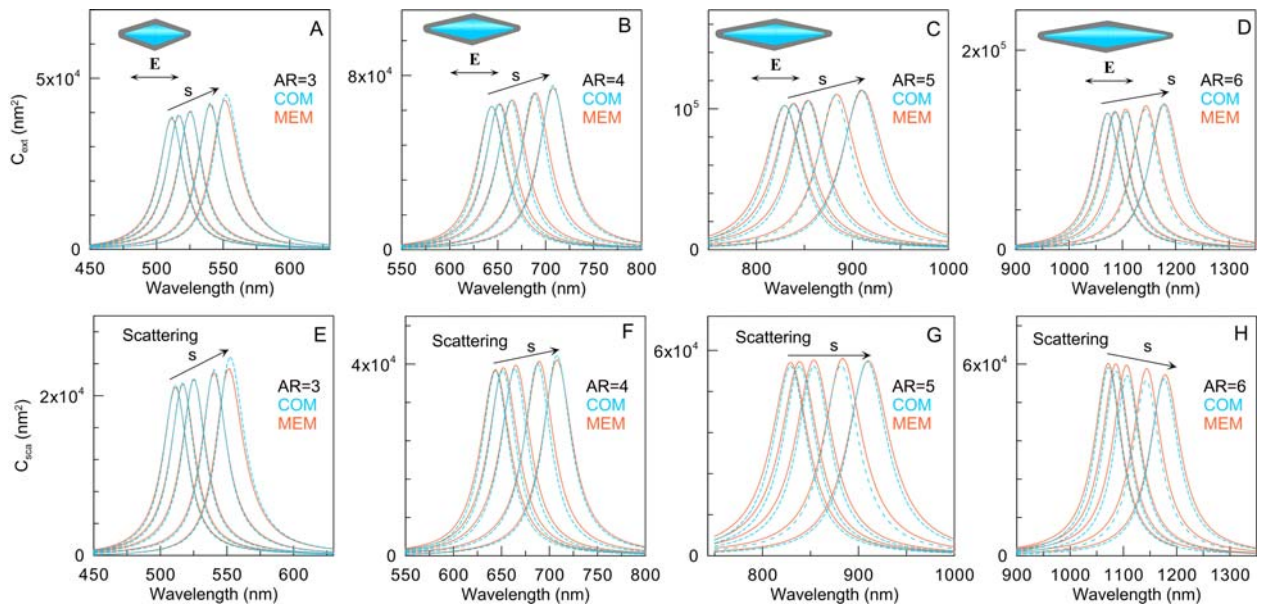


**Figure 15.** Extinction (A-D) and scattering (E-H) spectra were calculated by MEM (orange) and COMSOL (blue) for coated rounded silver bipyramids with a constant width of 30 nm and aspect ratios from 3 to 6. The shell thicknesses are 0, 1, 3, 10, and 30 nm.

## Conclusions

We have extended the MEM approximation previously developed for bare plasmonic nanoparticles to the coated ones. Remarkably, our MEM+DEM extension requires no additional numerical simulations to obtain analytical models for multilayered nanostructures. Actually, it is sufficient to find an analytical model for specific particle morphology and then apply DEM to extend the solution for a multilayered structure. We have found some disagreement between MEM+DEM spectra and numerical ones for sharp tip-shaped particles like bicones. However, our method works almost perfectly for bipyramide models with realistic rounding of both tips

and bases. In line with the original MEM theory<sup>20</sup>, the MEM+DEM approach can be easily applied to other particle shapes like ellipsoids, cubes, nanocages, etc. Due to its simplicity and reasonable accuracy, the developed analytical models can find valuable applications in machine learning to predict various plasmonic responses from coated particles, such as UV-vis extinction and scattering spectra, SERS, and MEF enhancement.

### **Acknowledgments**

This research was supported by the Russian Science Foundation (project no. 24-22-00017).

**Supporting Information.** Section S1: MEM parameters for selected particle shapes; Figures S1-S4. Section S2: Additional extinction and scattering spectra of bare and coated gold and silver nanorods, nanodisks, nanotriangles, bicones, and bipyramids; Figures S5-S16.

### **References and notes**

(1) Liz-Marzán L. (Ed.). Colloidal Synthesis of Plasmonic Nanometals. Jenny Stanford Publishing: New York, 2021.

(2) Lee J.W., Choi S.-R., Heo J.H. Simultaneous stabilization and functionalization of gold nanoparticles via biomolecule conjugation: progress and perspectives. ACS Appl. Mater. Interfaces, 2021, 13 (36), pp. 42311–42328, DOI: 10.1021/acsami.1c10436

(3) Arcos Rosero W.A., Bueno Barbezan A., Daruich de Souza C., Chuery Martins Rostelato M.E. Review of advances in coating and functionalization of gold nanoparticles: from theory to biomedical application. Pharmaceutics, 2024, 16 (2), art. no. 255, DOI: 10.3390/pharmaceutics16020255

(4) Patil T., Gambhir R., Vibhute A., Tiwari A.P. Gold nanoparticles: synthesis methods, functionalization and biological applications. J. Cluster Sci., 2023, 34 (2), 705–725 DOI: 10.1007/s10876-022-02287-6

(5) Zhang D., Gökce B., Barcikowski S. Laser Synthesis and processing of colloids: fundamentals and applications. *Chem. Rev.*, 2017, 117 (5), 3990–4103.

(6) Karnwal A., Kumar Sachan R.S., Devgon I., Devgon J., Pant G., Panchpuri M., Ahmad A., Alshammari M.B., Hossain K., Kumar G. Gold nanoparticles in nanobiotechnology: from synthesis to biosensing applications. *ACS Omega*, 2024, 9 (28), 29966–29982, DOI: 10.1021/acsomega.3c10352

(7) Selim A.A., Sakr T.M., Essa B.M. Gold nanoparticles: synthesis, functionalization and biomedical applications especially in cardiovascular therapy. *Pharm. Chem. J.*, 2023, 57 (1), 29–39, DOI: 10.1007/s11094-023-02847-8

(8) Bucharskaya AB, Khlebtsov NG, Khlebtsov BN, Maslyakova GN, Navolokin NA, Genin VD, Genina EA, Tuchin VV. Photothermal and photodynamic therapy of tumors with plasmonic nanoparticles: challenges and prospects. *Materials (Basel)*, 2022, 15(4), 1606. doi: 10.3390/ma15041606.

(9) Damani M., Jadhav M., Joshi R., Singh B.P., Momin M.M., Ningthoujam R.S., Khan T. Advances in gold nanoparticles: synthesis, functionalization strategies, and theranostic applications in cancer. *Critical Reviews in Therapeutic Drug Carrier Systems*, 2024, 41 (6), 1–56, DOI: 10.1615/CritRevTherDrugCarrierSyst.2024046712

(10) Tan K.F., In L.L.A., Vijayaraj Kumar P. Surface functionalization of gold nanoparticles for targeting the tumor microenvironment to improve antitumor efficiency. *ACS Appl. Bio Mater.*, 2023, 6 (8), 2944–2981, DOI: 10.1021/acsbm.3c00202

(11) Du X., Zhao M., Jiang L., Pang L., Wang J., Lv Y., Yao C., Wu R. A mini-review on gene delivery technique using nanoparticles-mediated photoporation induced by nanosecond

pulsed laser. *Drug Deliv.*, 2024, 31 (1), 2306231.  
<https://doi.org/10.1080/10717544.2024.2306231>

(12) Amina S.J., Guo B. A review on the synthesis and functionalization of gold nanoparticles as a drug delivery vehicle. *Int. J. Nanomedicine*, 2020, 15, 9823–9857, DOI: 10.2147/IJN.S279094

(13) Dykman L. A.; Khlebtsov N. G. Immunological properties of gold nanoparticles. *Chem. Sci.* 2017, 8, 1719–1735.

(14) Taha R.H. Green synthesis of silver and gold nanoparticles and their potential applications as therapeutics in cancer therapy; a review. *Inorg. Chem. Commun.*, 2022, 143, art. no. 109610, DOI: 10.1016/j.inoche.2022.109610

(15) Zheng J., Cheng X., Zhang H., Bai X., Ai R., Shao L., Wang J. Gold nanorods: the most versatile plasmonic nanoparticles. *Chem. Rev.* 2021, 121, 13342–13453.

(16) Myroshnychenko V., Rodríguez-Fernández J., Pastoriza-Santos I., Funston A. M., Novo C., Mulvaney P., Liz-Marzán L. M., García de Abajo F. J. Modelling the optical response of gold nanoparticles. *Chem. Soc. Rev.*, 2008, 37, 1792–1805.

(17) Khlebtsov N. G., Zarkov S. V. Analytical modeling of coated plasmonic particles. *J. Phys. Chem. C*, 2024, 128, 15029–15040.

(18) Khlebtsov N. G., Le Ru E. C. Analytical solutions for the surface and orientation averaged SERS enhancement factor of small plasmonic particles. *J. Raman Spectrosc.*, 2021, 52, 285–295.

(19) Khlebtsov N.G. T-matrix method in plasmonics: an overview. *J. Quant. Spectrosc. Radiat. Transfer*, 2013, 123, 184–217.

- (20) Yu R., Liz-Marzán L. M., García de Abajo F. J. Universal analytical modeling of plasmonic nanoparticles. *Chem. Soc. Rev.*, 2017, 46, 6710–6724.
- (21) Ciraci C., Urzhumov Y., Smith D. R. Far-field analysis of axially symmetric three-dimensional directional cloaks. *Opt. Express* 2013, 21, 9397–9406.
- (22) Gladyshev S., Pashina O., Proskurin A., Nikolaeva A., Sadrieva Z., Bogdanov A., Petrov M., Frizyuk K. Fast simulation of light scattering and harmonic generation in axially symmetric structures in COMSOL. *ACS Photoics*, 2024, 11, 404–418.
- (23) Khlebtsov N. G. Extinction and scattering of light by nonspherical particles in absorbing media. *J. Quant. Spectr. Radiat. Transfer*, 2022, 280, 108069.
- (24) Olmon R. L., Slovick B., Johnson T. W., Shelton D., Oh S.-H., Borema G. D., Raschke M. B. Optical dielectric function of gold. *Phys. Rev. B*, 2012, 86, 235147.
- (25) Drude, P. Über die Beziehung der Dielectricitätsconstanten zum optischen Brechungsexponenten. *Ann. der Physik*, 1893, 284(3), 536-545.
- (26) Bohren C. F., Huffman D. R. *Absorption and scattering of light by small particles*, Wiley: New York, 1983.
- (27) Sönnichsen C., Franzl T., Wilk T., von Plessen G., Feldmann J., Wilson O., Mulvaney P. Drastic reduction of plasmon damping in gold nanorods. *Phys. Rev. Lett.*, 2002, 88, 077402.
- (28) Kreibig U., Genzel L. Optical absorption of small metallic particles. *Surface Sci.*, 1985, 156, 678–700.
- (29) Novo C., Gomez D., Perez-Juste J., Zhang Z., Petrova H., Reismann M., Mulvaney P., Hartland G. V. Contributions from radiation damping and surface scattering to the linewidth of

the longitudinal plasmon band of gold nanorods: a single particle study. *Phys. Chem. Chem. Phys.*, 2006, 8, 3540–3546.

(30) Hövel H., Fritz S., Hilger A., Kreibig U., Vollmer M. Width of cluster plasmon resonances: bulk dielectric functions and chemical interface damping. *Phys. Rev. B*, 1993, 48, 18178–18188.

(31) Foerster B., Joplin A., Kaefer K., Celiksoy S., Link S., Sönnichsen C. Chemical interface damping depends on electrons reaching the surface. *ACS Nano*, 2017, 11, 2886–2893.

(32) Foerster B., Spata V. A., Carte E. A., Sönnichsen C., Link S. Plasmon damping depends on the chemical nature of the nanoparticle interface. *Sci. Adv.*, 2019, 5, eaav0704.

(33) Meier M., Wokaun A. Enhanced fields on large metal particles: dynamic depolarization. *Opt. Lett.*, 1983, 8, 581–583

(34) Moroz A. Depolarization field of spheroidal particles. *J. Opt. Soc. Am. B*, 2009, 26, 517–527.

(35) Jackson J. D. *Classical electrodynamics*, 3rd ed. Wiley: New York, 1999.

(36) Pipolo S., Corni S. Real-time description of the electronic dynamics for a molecule close to a plasmonic nanoparticle. *J. Phys. Chem. C*, 2016, 120, 28774–28781.

(37) Marcheselli J., Chateau D., Lerouge F., Baldeck P., Andraud C., Parola S., Baroni S., Corni S., Garavelli M., Rivalta I. Simulating plasmon resonances of gold nanoparticles with bipyramidal shapes by boundary element methods. *J. Chem. Theory Comput.*, 2020, 16, 3807–3815.

- (38) Kuwata H., Tamaru H., Esumi K., Miyano K. Resonant light scattering from metal nanoparticles: Practical analysis beyond Rayleigh approximation. *Appl. Phys. Lett.*, 83, 4625 (2003); DOI: 10.1063/1.1630351
- (39) Fuchs R. Theory of the optical properties of small cubes. *Phys. Lett. A*, 1974, 48 (5), 353–354.
- (40) Davis T. J., Gómez D. E. Colloquium: An algebraic model of localized surface plasmons and their interactions. *Rev. Mod. Phys.*, 2017, 89, 011003
- (41) Chen H., Shao L., Li Q., Wang J. Gold nanorods and their plasmonic properties. *Chem. Soc. Rev.*, 2013, 42, 2679–2724.
- (42) Eck D., Helm C. A., Wagner N. J., Vaynberg K. A. Plasmon resonance measurements of the adsorption and adsorption kinetics of a biopolymer onto gold nanocolloids. *Langmuir*, 2001, 17, 957–960. Errata: *Langmuir*, 2007, 23, 9522.
- (43) Khlebtsov N. G. Optical models for conjugates of gold and silver nanoparticles with biomacromolecules. *J. Quant. Spectrosc. Radiat. Transfer*, 2004, 89, 143–153.
- (44) Khlebtsov B. N., Khlebtsov N. G. Multipole plasmons in metal nanorods: Scaling properties and dependence on the particle size, shape, orientation, and dielectric environment. *J. Phys. Chem. C*, 2007, 111 (32), 11516–11527.
- (45) Kondorskiy A. D., Mekshun A. V. Effect of geometric parameters of metallic nanoprisms on the plasmonic resonance wavelength. *J. Russ. Laser Res.*, 2023, 44 (6), 627–636.
- (46) Kluitmann J., Csáki A., Fritzsche W., Köhler J. M. Tuning the growth pattern of triangular silver nanoplates from lateral to vertical by secondary metal addition. *ChemPhysChem*, 2024, e202400823 (1 of 8), doi.org/10.1002/cphc.202400823.

- (47) Lee J.-H., Gibson K.J., Chen G., Weizmann Y. Bipyramid-templated synthesis of monodisperse anisotropic gold nanocrystals. *Nat. Commun.*, 2015, 6, art. no. 7571, DOI: 10.1038/ncomms8571
- (48) Sánchez-Iglesias A., Winckelmans N., Altantzis T., Bals S., Grzelczak M., Liz-Marzán L.M. High-yield seeded growth of monodisperse pentatwinned gold nanoparticles through thermally induced seed twinning. *J. Am. Chem. Soc.*, 2017, 139 (1), pp. 107–110, DOI: 10.1021/jacs.6b12143
- (49) Chow T.H., Li N., Bai X., Zhuo X., Shao L., Wang J. Gold nanobipyramids: an emerging and versatile type of plasmonic nanoparticles. *Acc. Chem. Res.*, 2019, 52 (8), pp. 2136–2146, DOI: 10.1021/acs.accounts.9b00230
- (50) Nguyen A.L., Griffin Q.J., Wang A., Zou S., Jing H. Optimization of the surfactant ratio in the formation of penta-twinned seeds for precision synthesis of gold nanobipyramids with tunable plasmon resonances. *J. Phys. Chem. C*, 2025, 129 (8), 4303–4312. DOI: 10.1021/acs.jpcc.4c08818
- (51) Montaña-Priede J.L., Sánchez-Iglesias A., Mezzasalma S.A., Sancho-Parramon J., Grzelczak M. Quantifying shape transition in anisotropic plasmonic nanoparticles through geometric inversion. application to gold bipyramids. *J. Phys. Chem. Letters*, 2024, 15 (14), 3914–3922, DOI: 10.1021/acs.jpcclett.4c00582
- (52) Khlebtsov N. G. Optical models for conjugates of gold and silver nanoparticles with biomacromolecules. *J. Quant. Spectrosc. Radiat. Transfer*, 2004, 89, 143–153.
- (53) Liu F., Robinson W.L., Kirscht T., Fichthorn K.A., Jiang S. Biobased polymers enabling the synthesis of ultralong silver nanowires and other nanostructures. *Nano Lett.*, 2024, 24 (45), 14381–14388, DOI: 10.1021/acs.nanolett.4c041301



(54) Wiley B. J., Xiong Y., Li Z.-Y., Yin Y., Xia Y. Right bipyramids of silver: a new shape derived from single twinned seeds. *Nano Lett.*, 2006, 6 (4), 765–768.

(55) Tavakkoli Yarak M., Daqiqeh Rezaei S., Mirdha E., Tan Y.N. Synthesis and simulation study of right silver bipyramids via seed-mediated growth cum selective oxidative etching approach. *Part. Part. Syst. Charact.*, 2020 37 (5), art. no. 2000027, DOI: 10.1002/ppsc.202000027.

(56) Zhu Z., Wang X., Yu H., Zhou W., Wang Y., Han J., Guo F. Improved polyol syntheses of silver right bipyramids and nanorods: camphorquinone-mediated morphology control methods. *Cryst. Growth Des.*, 2023, 23 (3), 1455–1465, DOI: 10.1021/acs.cgd.2c01031

# Supporting Information

## Universal analytical modeling of coated plasmonic particles

Nikolai G. Khlebtsov<sup>1,2,\*</sup>, Sergey V. Zarkov<sup>1,3</sup>

<sup>1</sup>Institute of Biochemistry and Physiology of Plants and Microorganisms, "Saratov Scientific Centre of the Russian Academy of Sciences," 13 Prospekt Entuziastov, Saratov 410049, Russia

<sup>2</sup>Saratov State University, 83 Ulitsa Astrakhanskaya, Saratov 410012, Russia

<sup>3</sup>Institute of Precision Mechanics and Control, "Saratov Scientific Centre of the Russian Academy of Sciences," 24 Ulitsa Rabochaya, Saratov 410028, Russia

\*To whom correspondence should be addressed. E-mail: (NGK) khlebtsov@ibppm.ru

### RECEIVED DATE

### Section 1. MEM parameters for selected particle shapes

For rods and discs, MEM parameters coincide with those given in Ref. [1]. Coated rods and disks' geometrical sizes should be increased by twice the shell thickness  $2s$ . Accordingly, the

aspect ratios of coated rods and disks are calculated as  $AR_2 = \frac{L_1 + 2s}{d_1 + 2s}$  and  $AR_2 = \frac{D_1 + 2s}{t_1 + 2s}$ ,

respectively. Below, the symbol  $h$  designates the generalized aspect ratio  $AR_1$  for the metal core and  $AR_2$  for shell. It should be emphasized here that we use the same MEM functions for metal cores and shells due to DEM philosophy.

#### 1.1 Rods

$$\eta_1(h) = -1.73h^{1.45} - 0.296, \quad a_{12}(h) = 6.92 / [1 - \eta_1(h)], \quad a_{14}(h) = -11h^{-2.49} - 0.0868, \quad (S1)$$

$$V_1^m / V_{NR} = 0.896, V_{NR} / L_1^3 = \frac{\pi(3h-1)}{12h^3}. \quad (\text{S2})$$

## 1.2. Disks

$$\eta_1(h) = -1.36h^{0.872} - 0.479, a_{12}(h) = 7.05 / [1 - \eta_1(h)], a_{14}(h) = -10.9h^{-0.98}, \quad (\text{S3})$$

$$V_1^m / V_{ND} = 0.944, V_{ND} / L_1^3 = \frac{\pi}{24h^3} [4 + 3(h-1)(2h + \pi - 2)]. \quad (\text{S4})$$

## 1.3. Triangle prism

The generalized aspect ratios of bare and coated nanoprisms are characterized by similar expressions in  $AR_i \equiv h_i = L_i / t_i$ ,  $i = 1, 2$ , where the indices 1 and 2 stand for the metal core and shell, respectively;  $L_2 = L_1 + 2\sqrt{3}s$ , and  $t_2 = t_1 + 2s$ . Here,  $t_1$  and  $t_2$  designate the bare and coated prism thicknesses, respectively. Note that both lengths here are given in terms of nonrounded particles. By fitting MEM spectra to COMSOL ones, we derived the following MEM parameters for rounded triangle nanoprisms:

$$\eta_1(h) = -3.2483 - 1.2047h + 0.00632112h^2, \quad (\text{S5})$$

$$a_{12}(h) = 5.57 / [1 - \eta_1(h)], a_{14}(h) = -6.83 / [1 - \eta_1(h)], \quad (\text{S6})$$

$$V_1^m / V_{NT} = 0.55 + 0.155 [1 - e^{-(h-2)^5}], \quad (\text{S7})$$

$$V_{NT} / L_1^3 = \frac{\sqrt{3}}{4h} - \frac{(h+1)^2}{1600h^2} \left( \frac{3\sqrt{3} - \pi}{h} + 6 \left( 1 - \frac{1}{4}\pi \right) \right). \quad (\text{S8})$$

In all the above equations, the symbol  $h$  stands for the aspect ratio of rounded core ( $AR_1$ ) or shell ( $AR_2$ ), respectively.

In Eq. (S8), the nanoprism volume  $V_{NT}$  was calculated by considering rounding for three base corners and six lateral edges. The rounding radius equals to  $r = (1 + 1/AR) \times L / 40$  [1]. Below, we provide a short derivation.

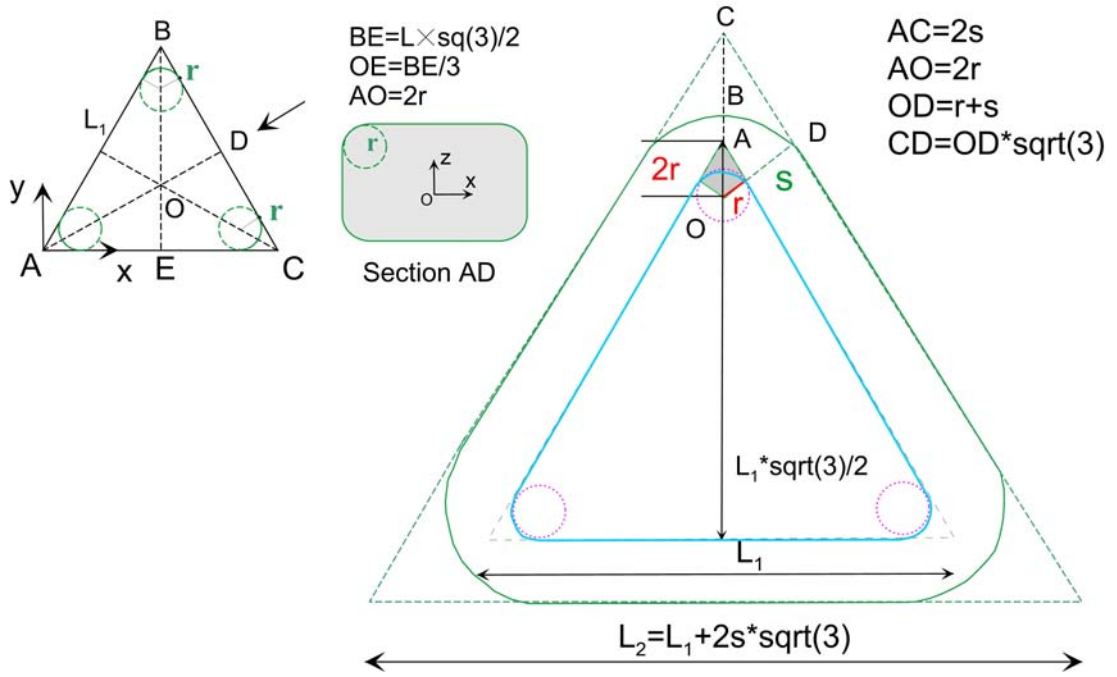


**Figure S1.** Scheme of the rounded bare and coated triangle prisms

Let's start with three corners in the triangle plane (Figure S1).

$S_0 = (L/2) \times L\sqrt{3}/2 = L^2\sqrt{3}/4$  is the area of the initial triangle without rounding

$S_1 = 2 \times (r/2)r\sqrt{3} = r^2\sqrt{3}$  is the area of two shadowed triangles at the upper corner

$S_2 = \pi r^2/3$  is the area of the shadowed portion of the corner circle

The total area of three corner portions that should be excluded from the initial triangle is

$$S_{exc} = S_1 - S_2 = 3 \times r^2(\sqrt{3} - \pi/3) = r^2(3\sqrt{3} - \pi)$$

The total area of the rounded triangle

$$S_r = S_0 - S_{exc} = \left[ L^2\sqrt{3}/4 - r^2(3\sqrt{3} - \pi) \right]$$

Considering the above expression for the rounding radius  $r$  and multiplying by the particle thickness, we obtain the total volume of the triangle prism with rounded corners:

$$V_{rc} = \left[ L^2\sqrt{3}/4 - (1 + 1/AR)^2 \times L^2/1600 \times (3\sqrt{3} - \pi) \right] L/AR$$

Now, we consider six lateral edges. Because of rounding, we have to exclude six volumes between the square area  $r^2$  and  $1/4$  of the circle area  $\pi r^2$  multiplied by six edge lengths  $L$ :

$$V_{1exc} = 6L \times (r^2 - 1/4\pi r^2) = 6L^3(1 + 1/AR)^2(1 - \pi/4)/1600.$$

A similar expression can be written for three angular edges of a thickness  $t$ :

$$V_{2exc} = 3t \times (r^2 - 1/4\pi r^2) = (3/AR)L \times (r^2 - 1/4\pi r^2) = 3L^3(1 + 1/AR)^2(1 - \pi/4)/1600AR$$

As we consider thin prisms with  $AR > 3$ , the last contribution  $V_{2exc}$  is one order less than  $V_{1exc}$ . Thus, one can neglect  $V_{2exc}$  compared to  $V_{1exc}$ .

Combining all previous results, we arrive at the final expression (S8) for the rounded triangle prism volume (remember that  $h = AR$ ). Note that the first term coincides with that given in Fig. 3 caption by Yu et al. [1]:

$$\frac{V^{Yu}}{L^3} = \frac{0.433}{AR} - \frac{0.00544}{AR^2}, \quad (S9)$$

but the other terms differ. However, as the rounding radius is small, the above difference should not affect the main conclusions made from calculations by Yu et al. [1]

It follows from Figure 1 that the volume of a rounded coated nanoprism can be calculated by the above Eq. (S8) with  $L \equiv L_2 = L_1 + 2\sqrt{3}s$  and  $h = AR_2 = L_2 / (t_1 + 2s)$

## 1.4. Rounded bicone

### 1.4.1. Geometrical parameters

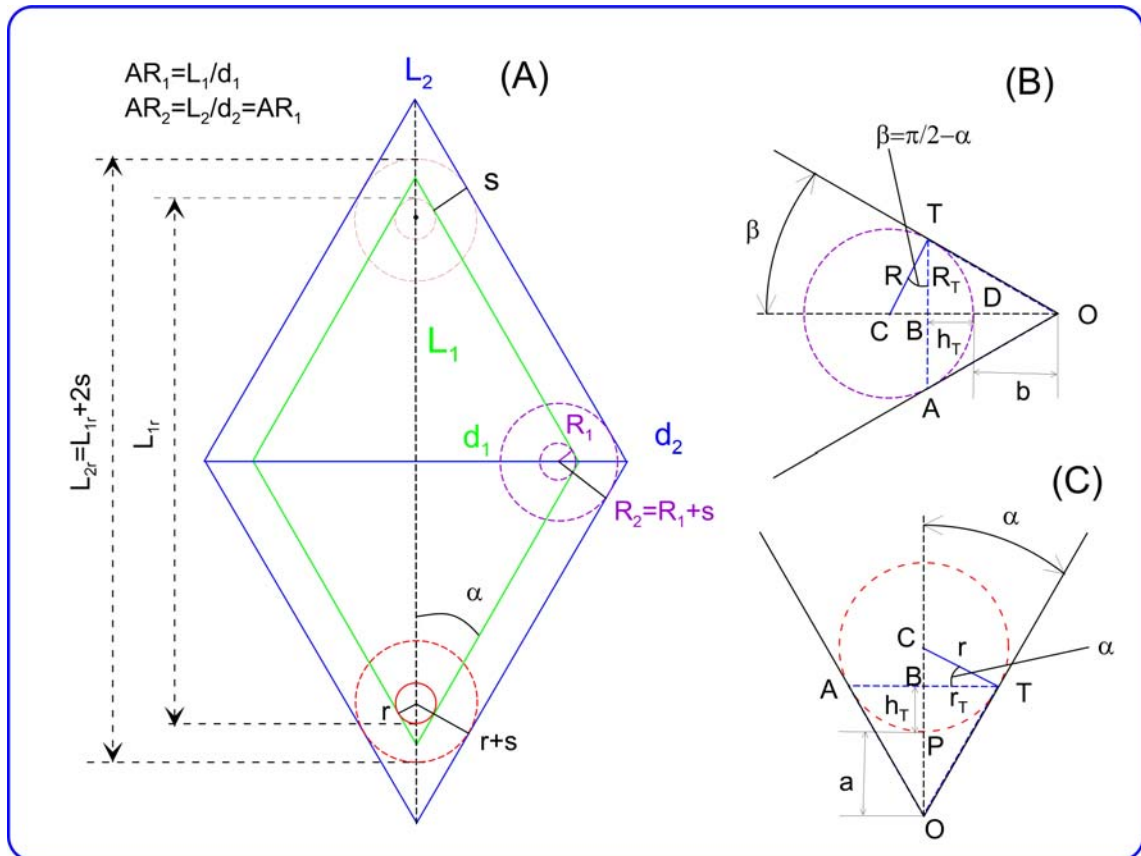


**Figure S2.** Scheme of the rounded bare and coated bicones

The size and shape of the initial bicone (nonrounded metal core) is characterized by the total  $L_1$  length, diameter  $d_1$ , and aspect ratio  $AR_1 = L_1 / d_1$ . The rounded core is characterized by the rounded length  $L_{1r} = p_1$  and the rounded base diameter  $d_{1r}$ . The nonrounded shell bicone is characterized by similar parameters  $L_2$ ,  $d_2$ , and  $AR_2 = L_2 / d_2 = AR_1$ . From Figure 2, we have

$$L_2 = L_1 + 2s / \sin \alpha = L_1 + 2s\sqrt{1 + AR_1^2}, \quad (S10)$$

$$d_2 = d_1 + 2s / \cos \alpha = d_1 + 2s\sqrt{1 + AR_1^2} / AR_1. \quad (S11)$$

The constant shell thickness is  $s$ ; therefore, the rounded shell length and diameter are  $L_{2r} \equiv p_2 = p_1 + 2s \equiv L_{1r} + 2s$  and  $d_{2r} = d_{1r} + 2s$ , respectively.

The rounding radii for metal and coated bicones are  $r_1$  and  $r_2 = r_1 + s$ , respectively. Similarly, the rounding radii of the bases are  $R_1$  and  $R_2 = R_1 + s$ , respectively. The rounded lengths and diameter of the core are

$$L_{1r} = p_1 = L_1 - 2a_1, \quad (S12)$$

$$d_{1r} = d_1 - 2b_1, \quad (S13)$$

where

$$a_1 = qr_1, \quad b_1 = gR_1 \quad (S14)$$

$$q = (1 - \sin \alpha) / \sin \alpha = \sqrt{1 + AR^2} - 1, \quad (S15)$$

$$g = (1 - \cos \alpha) / \cos \alpha = \sqrt{AR^{-2} + 1} - 1 \quad (S16)$$

$$\alpha = \arctg(1 / AR_1), \quad \sin \alpha = 1 / \sqrt{1 + AR^2}, \quad \cos \alpha = AR / \sqrt{1 + AR^2}. \quad (S17)$$

Note that the aspect ratios of rounded core and shell differ from their initial (nonrounded) counterparts

$$AR_{1r} = \frac{L_{1r}}{d_{1r}} = \frac{L_1 - 2a_1}{d_1 - 2b_1} \leq \frac{L_1}{d_1}, \quad (S18)$$

$$AR_{2r} = \frac{L_{2r}}{d_{2r}} = \frac{L_{1r} + 2s}{d_{1r} + 2s} \leq \frac{L_{1r}}{d_{1r}} \quad (S19)$$

#### 1.4.2. Calculation of the rounded bicone volume

The volume of initial bicone with the total length  $L$  and diameter  $d$  equals

$$V_i = \frac{2}{3} \pi (d_i / 2)^2 \frac{L_i}{2} = \frac{\pi L_i^3}{12 AR_i^2}, \quad AR_i = L_i / d_i, \quad i = 1, 2, \quad (S20)$$

where the indices 1 and 2 stand for the core and shell, respectively. To exclude the rounded tip volumes, we have to substrate two volumes located between the spherical segment ATP and ATO cone (Figure 2C):

$$V_{exc}^{tips} = \frac{\pi}{3} (2r_T^2 a - r_T^2 h_T - h_T^3), \quad (S21)$$

$$h_T = r(1 - \sin \alpha), \quad (S22)$$

$$r_T = r \cos \alpha, \quad (S23)$$

where the rounding radius  $r$  can be  $r_1$  or  $r_2$ . After some algebra, we get

$$V_{exc}^{tip} = \frac{2\pi}{3} r^3 \frac{(1 - \sin \alpha)^2}{\sin \alpha}. \quad (S24)$$

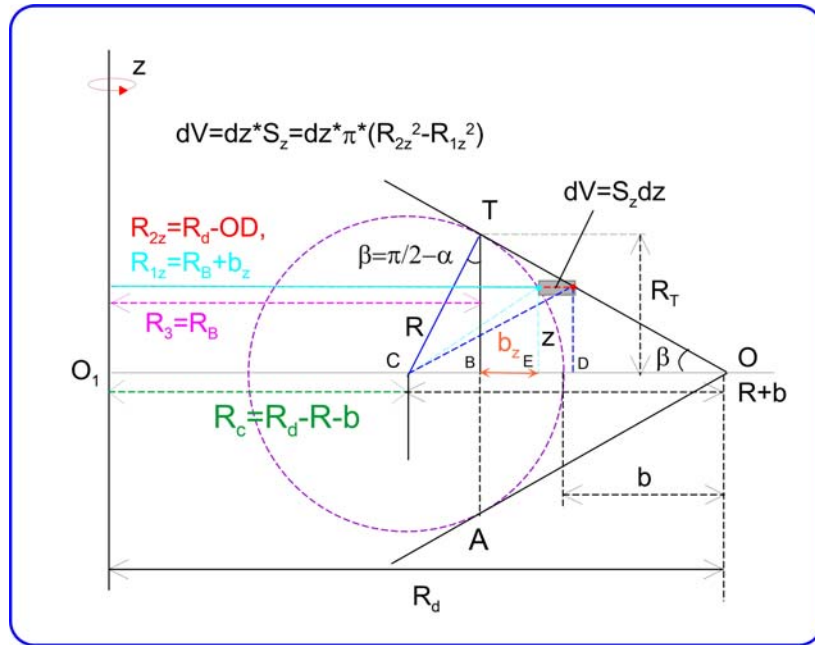


**Figure S3.** Calculating the base excluded volume.

For a rounded base, the excluded volume can be calculated as (see Figure S3)

$$V_{exc}^{base} = V_{21} - V_{11} = 2\pi \int_0^{R_T} (R_{2z}^2 - R_{1z}^2) dz. \quad (S25)$$

where the following relations define all related quantities:

$$R_{2z}^2 = [R_d - z \operatorname{tg}(\alpha)]^2 = R_d^2 - 2R_d \operatorname{tg}(\alpha)z + z^2 \operatorname{tg}^2(\alpha),$$

$$R_{1z}^2 = (R_3 + b_z)^2 = \left( R_3 - \sqrt{R^2 - R_T^2} + \sqrt{R^2 - z^2} \right)^2 = \left( R_3 - R_4 + \sqrt{R^2 - z^2} \right)^2 = \left( R_{34} + \sqrt{R^2 - z^2} \right)^2$$

$$R_{2z}^2 - R_{1z}^2 = R_d^2 - 2R_d \operatorname{tg}(\alpha)z + z^2 \operatorname{tg}^2(\alpha) - R_{34}^2 - 2R_{34} \sqrt{R^2 - z^2} - R^2 + z^2$$

$$R_{2z}^2 - R_{1z}^2 = A - 2R_d \operatorname{tg}(\alpha)z + z^2 / \cos^2(\alpha) - 2R_{34} \sqrt{R^2 - z^2}$$

$$A = R_d^2 - R_{34}^2 - R^2, \quad R_{34} = R_3 - R_4 = R_3 - \sqrt{R^2 - R_T^2} = R_3 - R \cos \alpha$$

$$R_3 = R_B = R_C + R \sin \beta = R_d - R / \cos \alpha + R \cos \alpha = R_d - R \operatorname{tg} \alpha \sin \alpha$$

$$R_{34} = R_d - R \tan \alpha \sin \alpha + R \cos \alpha = R_d - R / \cos \alpha.$$

With using integral

$$\int_0^{R_T} \sqrt{R^2 - z^2} dz = \frac{R_T \sqrt{R^2 - R_T^2}}{2} + \frac{R^2}{2} \arcsin \frac{R_T}{R},$$

we get:

$$V_{21} = R_T \left[ R_d^2 - R_d R_T \tan(\alpha) + \frac{1}{3} R_T^2 \tan^2(\alpha) \right] \quad (\text{S26})$$

$$V_{11} = R_T \left[ R_{34}^2 + R^2 - \frac{1}{3} R_T^2 \right] + R_{34} \left[ R_T R \cos(\alpha) + R^2 \arcsin \frac{R_T}{R} \right] \quad (\text{S27})$$

$$V_{exc}^{base} = 2\pi (V_{11} - V_{21}) \quad (\text{S28})$$

After some algebra, we arrive at the final expression:

$$V_{exc}^{base} = 2\pi R^2 \left[ R_d (\tan \alpha - \alpha) + R \left( -\frac{\sin \alpha}{3} \left( 1 + \frac{2}{\cos^2 \alpha} \right) + \frac{\alpha}{\cos \alpha} \right) \right], \quad (\text{S29})$$

$$\alpha = \arctan \frac{1}{AR_1}. \quad (\text{S30})$$

Nothe, the angle  $\alpha$  is the same for the core and shell. In Eq. (S29), the rounding radius  $R$  can be  $R_1$  for the core and  $R_2 = R_1 + s$  for the shell.

The above analytical expressions for the rounded bicone volume were checked with a direct numerical integration by COMSOL.

For numerical simulations, we used the rounding radii  $r_i = L_i / 40AR_i = d_i / 40, i=1,2$  for the core and shell tips and  $R_i = d_i / 100, i=1,2$  for the core and shell bases. For metal bicones, this parametrization was used by Yu et al. [1].

### 1.4.3. MEM parameters for bare and coated rounded bicones.



The rounded bare and coated bicones volume is calculated as a difference between initial and excluded base and tip volumes.  $V_{BCr} = V_{BC} - (V_{exc}^{tip} + V_{exc}^{base})$ . All related expressions have been provided in the previous subsections 1.4.1-1.4.2. To calculate the modal volumes (mode 1), we used the following factorization model

$$V_1^m = V_{BCr} \times f_{Vh}(h_r) f_{Vs}(s), \quad (S31)$$

$$f_{Vh}(x) = 0.32259 + 0.086858x - 0.015968x^2 + 0.0013815x^3 - 4.55693E-005x^4, \quad (S32)$$

$$f_{Vs}(x) = \begin{cases} 1, & s = 0 \\ \exp(0.083478 + 0.033629x - 0.0057969x^2 - 0.0020217x^3), & x = \ln(s), 1 \leq s \leq 30 \end{cases}. \quad (S33)$$

The MEM parameters  $\eta_j^p(h_r)$  for the first mode  $j=1$  and longitudinal excitation along the bicone symmetry axis ( $p=l \equiv \parallel$ ) are calculated by the following factorized approximation

$$\eta_1 = -f_{\eta h}(h_r) \times f_{\eta s}(s), \quad (S34)$$

$$f_{\eta h}(x = h_r) = 0.29105 + 2.6267x + 0.84365x^2 - 0.0057085x^3 - 0.00043102x^4, \quad (S35)$$

$$f_{\eta s}(s) = \begin{cases} 1, & s = 0 \\ 1.29478s^{0.114969}, & 1 \leq s \leq 30 \end{cases}, \quad (S36)$$

Finally, the last two MEM parameters for the first longitudinal mode are [1]

$$\alpha_{12}(h_r) = \frac{1.34}{1 - \eta_1}, \quad \alpha_{11}(h_r) = -\frac{1.04}{1 - \eta_1}. \quad (S37)$$

In all the above equations,  $h_r$  stands for the aspect ratio of rounded core ( $AR_{1r}$ ) or shell ( $AR_{2r}$ ), respectively.

If the rounding radii of core and base are large enough, the functions  $f_{Vs}(s)$  and  $f_{\eta s}(s)$  can be replaced with 1, and the functions  $f_{Vh}(x)$  and  $f_{\eta h}(x)$  should be properly defined from the fitting to numerical data. In other words, the factorized MEM-F representations (S31) and (S34) are reduced to standard MEM ones.

## 1.5. Rounded bipyramid

The geometrical parameters of our rounded bipyramid (BP) model are based on the embedded bicone model. This model is characterized by the diameter of a circle inscribed in the pentagon of the base of the BP and its height coinciding with the height of the BP. It follows from experimental data (e.g., [2] and references therein) that the tip rounding radius  $R_{tip}$  increases with a decrease in the actual BP length  $L_{1r}$ . Similarly, the base rounding radius  $R_{base}$  also increases during the chemical etching. Unfortunately, in the theoretical model, the length of a rounded BP and its aspect ratio depend on the rounding radii, so we have a nonlinear relationship. To avoid this difficulty, we assume the linear relations between the rounding radii and the aspect ratio of the initial (nonrounded) BP

$$R_{tip} \text{ (nm)} = 2 + 2(6 - AR_1), 1 \leq AR_1 \leq 6, \quad (\text{S38})$$

$$R_{base} \text{ (nm)} = 16 - 2AR_1, \quad (\text{S39})$$

In our simulations, we fixed the inscribed bicone diameter as the BP width and varied the aspect ratio from 2 to 6. This resulted in a progressive decrease in the rounding radii, consistent with the experimental measurements presented in [2].

Given the bipyramid diameter, aspect ratio, and rounding radii (S36) and (S37), we numerically calculated the rounded BP volume and all geometrical parameters of the embedded bicone analytically. Then, we approximate the BP volume by a polynomial (Figure S4) of the rounded aspect ratio

$$V_{BP}(s=0) = -7486.03 + 18338.49AR_{1r} - 1433.54AR_{1r}^2, \quad (\text{S40})$$

where the shell thickness  $s$  is assumed to be zero. Then, for a given shell thickness  $s$ , we calculated analytically the ratio  $F_V(s) = V_{BCr}(s) / V_{BCr}(s=0)$ . Finally, the volume of a rounded coated BP was calculated as  $V_{BCr}(s) = F_V(s)V_{BCr}(s=0)$ . Panel B in Figure 4 illustrates the excellent accuracy of this approximation, better than 0.002%.

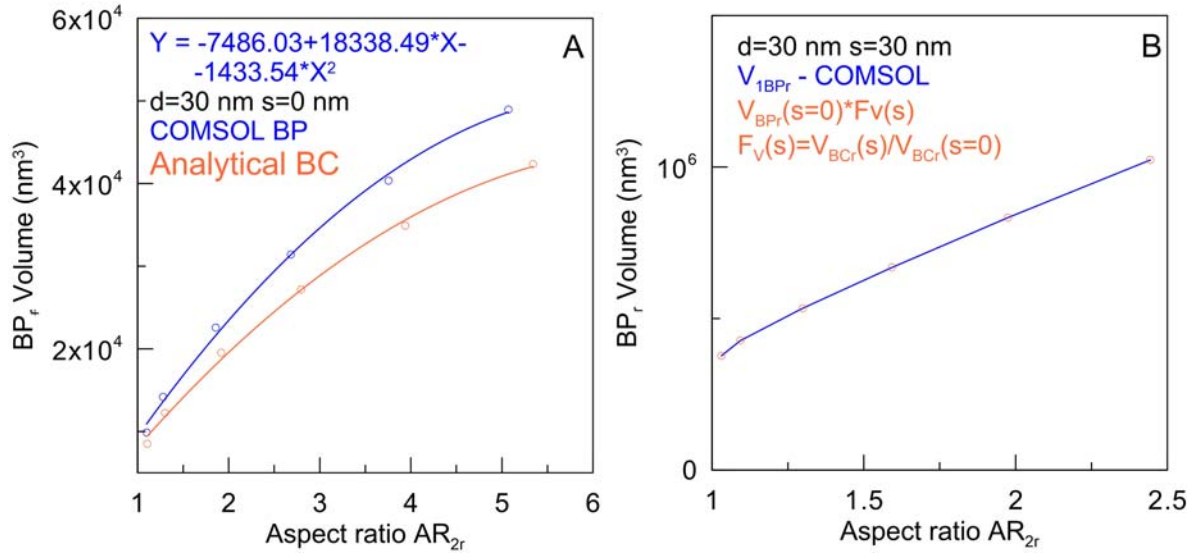


**Figure S4.** Polynomial approximation of the BP (blue, numerical) and BC (orange, analytical) as a function of the rounded bicone aspect ratio (A). Comparison of numerical (blue line) and analytical (orange dots)  $BP_r$  volumes.

With the rounded BP volume in hand, we calculated other MEM parameters as follows:

$$\eta_1(h_r) = -f_\eta(h_r), \quad (S41)$$

$$f_\eta(x) = -1.36762 + 3.0204378x + 0.09294389x^2 + 0.07895368x^3,$$

$$a_{12}(h_r) = 5.57 / [1 - \eta_1(h_r)], \quad a_{14}(h_{ir}) = -6.83 / [1 - \eta_1(h_{ir})], \quad (S42)$$

$$V_1^m = f_v(h_r)V_{BPr}, \quad (S43)$$

$$f_v(x) = 0.976704 - 0.0237377x - 0.00453238x^2.$$

For silver bipyramids, Eqs. (S41) and (S43) should be modified as follows:

$$\eta_1(h_r) = -f_\eta(h_r), \quad (S44)$$

$$f_\eta(x) = -0.323882 + 1.42211x + 1.01670x^2 - 0.129240x^3 + 0.0160452x^4,$$

$$V_1^m = f_v(h_r)V_{BPr}, \quad (S45)$$

$$f_v(x) = 0.519999 + 0.562648x - 0.279774x^2 + 0.0561240x^3 - 0.00413525x^4.$$

In all the above equations, the symbol  $h_r$  stands for the aspect ratio of rounded core ( $AR_{1r}$ ) or shell ( $AR_{2r}$ ), respectively.

**Section 2. Additional extinction and scattering spectra of bare and coated gold and silver nanorods, nanodisks, nanotriangles, bicones, and bipyramids.**

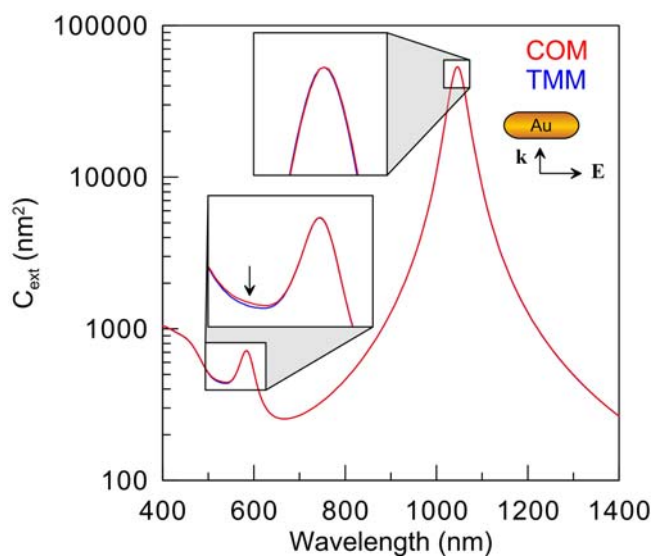


**Figure S5.** Comparison of extinction spectra calculated by COMSOL (2.5D, red curve COM) and T-matrix method (TMM, blue) for a longitudinal excitation of an AuNR with length 90 nm and diameter 15 nm. Both spectra have excellent agreement except for a slight difference near 550 nm. A small peak near 580 nm corresponds to the quadrupole excitation.

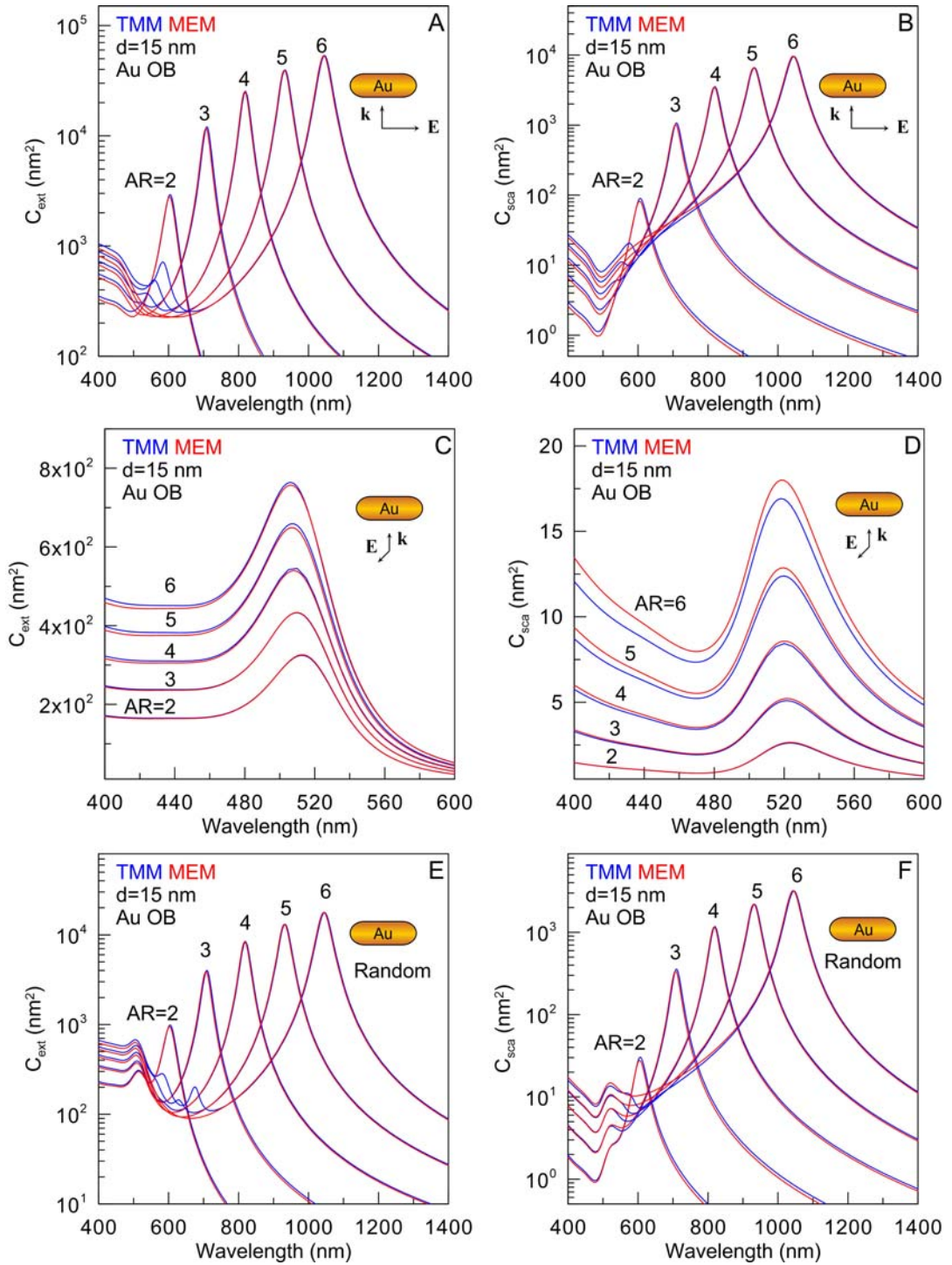


**Figure S6.** Comparison of extinction and scattering spectra calculated by the T-matrix method (TMM, blue) and MEM (red) for longitudinal (A, B) and perpendicular (C, D) excitations and for randomly oriented AuNRs (E, F) with length 90 nm and diameter 15 nm. There is excellent agreement between TMM and MEM spectra around main plasmonic peaks and satisfactory agreement for short wavelength perpendicular peaks except for quadrupole resonances that MEM cannot reproduce.

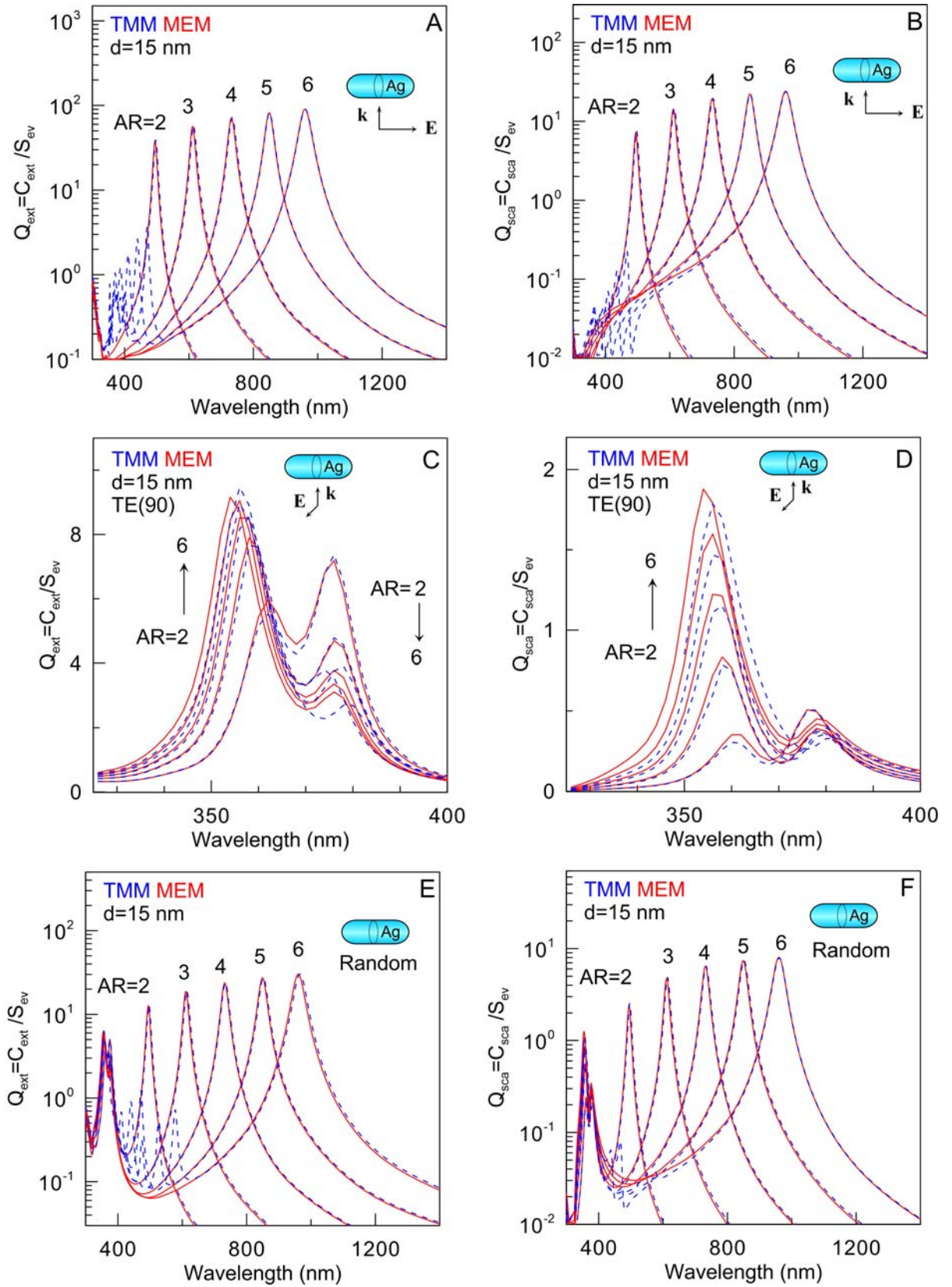


**Figure S7.** Comparison of extinction and scattering spectra calculated by the T-matrix method (TMM, blue) and MEM (red) for longitudinal (A, B) and perpendicular (C, D) excitations and

for randomly oriented AgNRs (E, F) with length 90 nm and diameter 15 nm. There is excellent agreement between TMM and MEM spectra around main plasmonic peaks in panels A, B, E, and F. Two minor peaks near 355 and 375 nm are reproduced by MEM with acceptable accuracy. In addition, spectra in panels A, B, E, and F exhibit multipole resonances that MEM cannot reproduce.

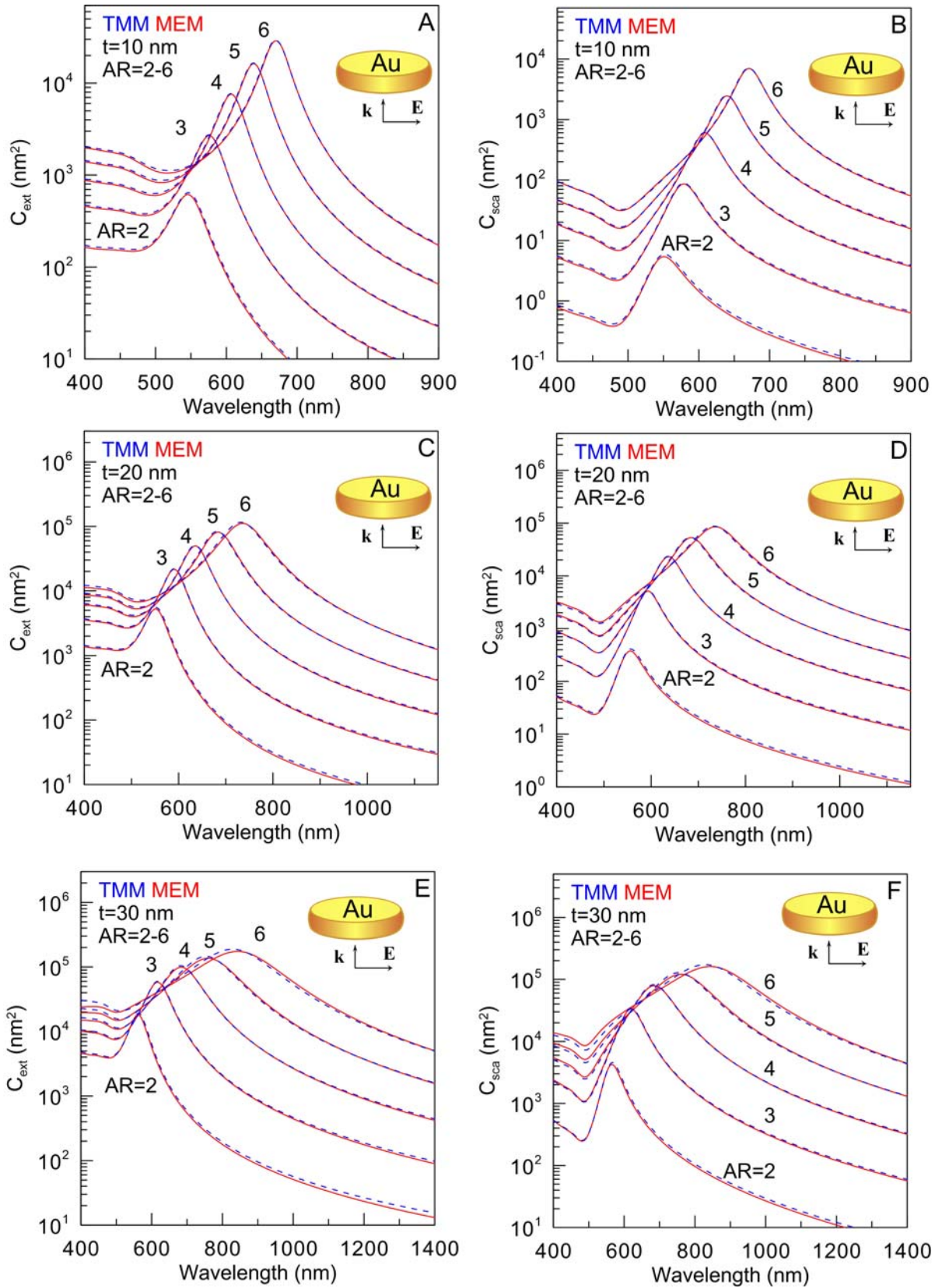


**Figure S8.** Comparison of extinction and scattering spectra calculated by the T-matrix method (TMM, blue) and MEM (red) for excitation along nanodisk diameter  $D$ . The disk thickness  $t$  is 10 (A, B), 20 (C, D), and 30 nm (E, F); the aspect ratio  $AR = D/t$  varies from 2 to 6. There is



excellent agreement between TMM and MEM spectra for disks of 10 and 20 nm thicknesses and some minor differences for thicknesses of 30 nm.

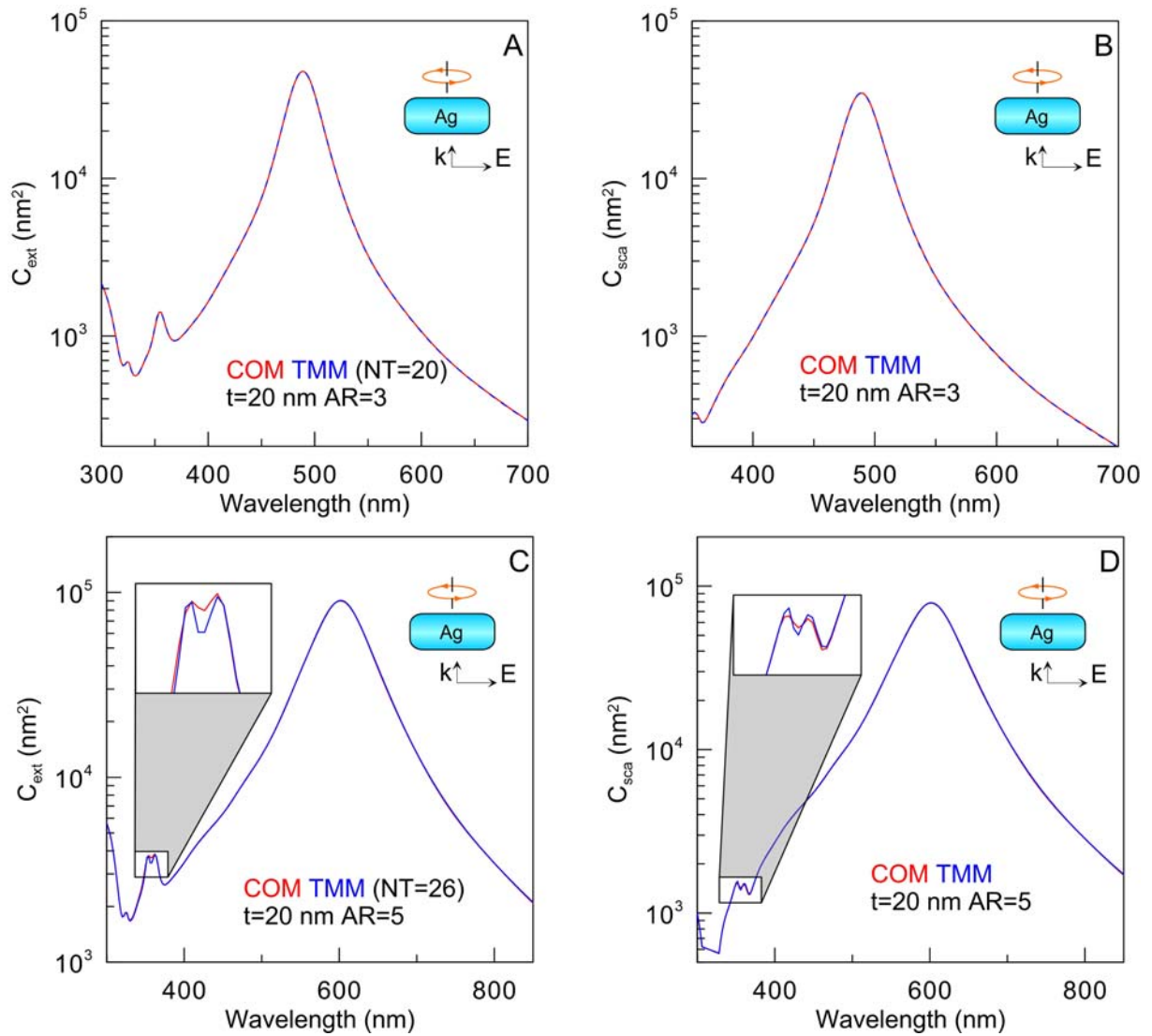


**Figure S9.** Comparison of extinction and scattering spectra calculated by COMSOL (2.5D, red curve COM) and T-matrix method (TMM, blue) for an in-plane excitation of an AgNR with a thickness of 20 nm and aspect ratio of 3 (A, B) and 5 (C, D). Both spectra have an excellent agreement for  $AR=3$  except for minor deviations within the 340-380 nm spectral band for  $AR=5$ .

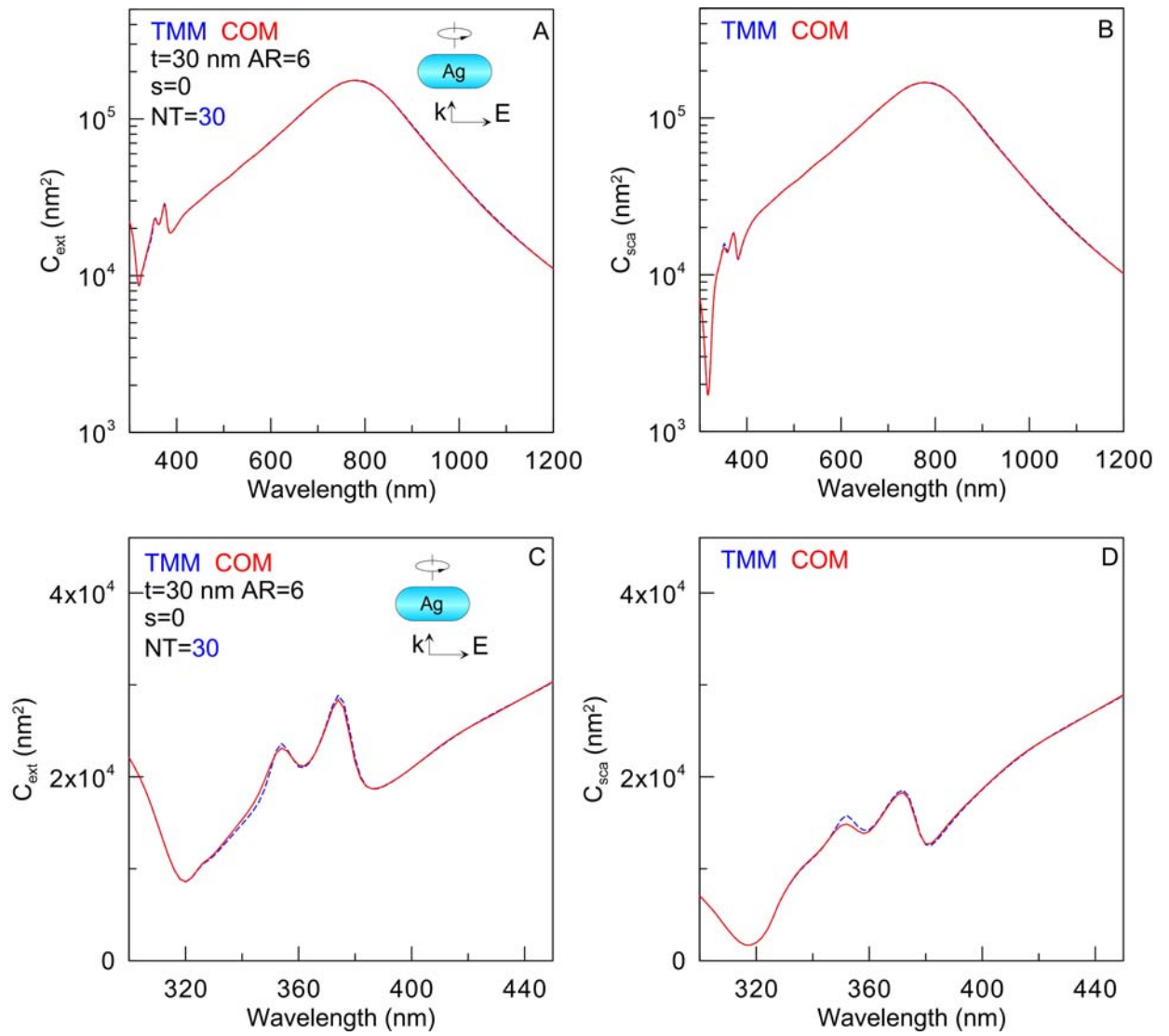


**Figure S10.** Extinction (A, C) and scattering (B, D) spectra for a thick 30×180 nm Ag disk calculated by TMM and COM. Panels C and D show minor differences between TMM and COM spectra for a 300-450 nm spectral band.

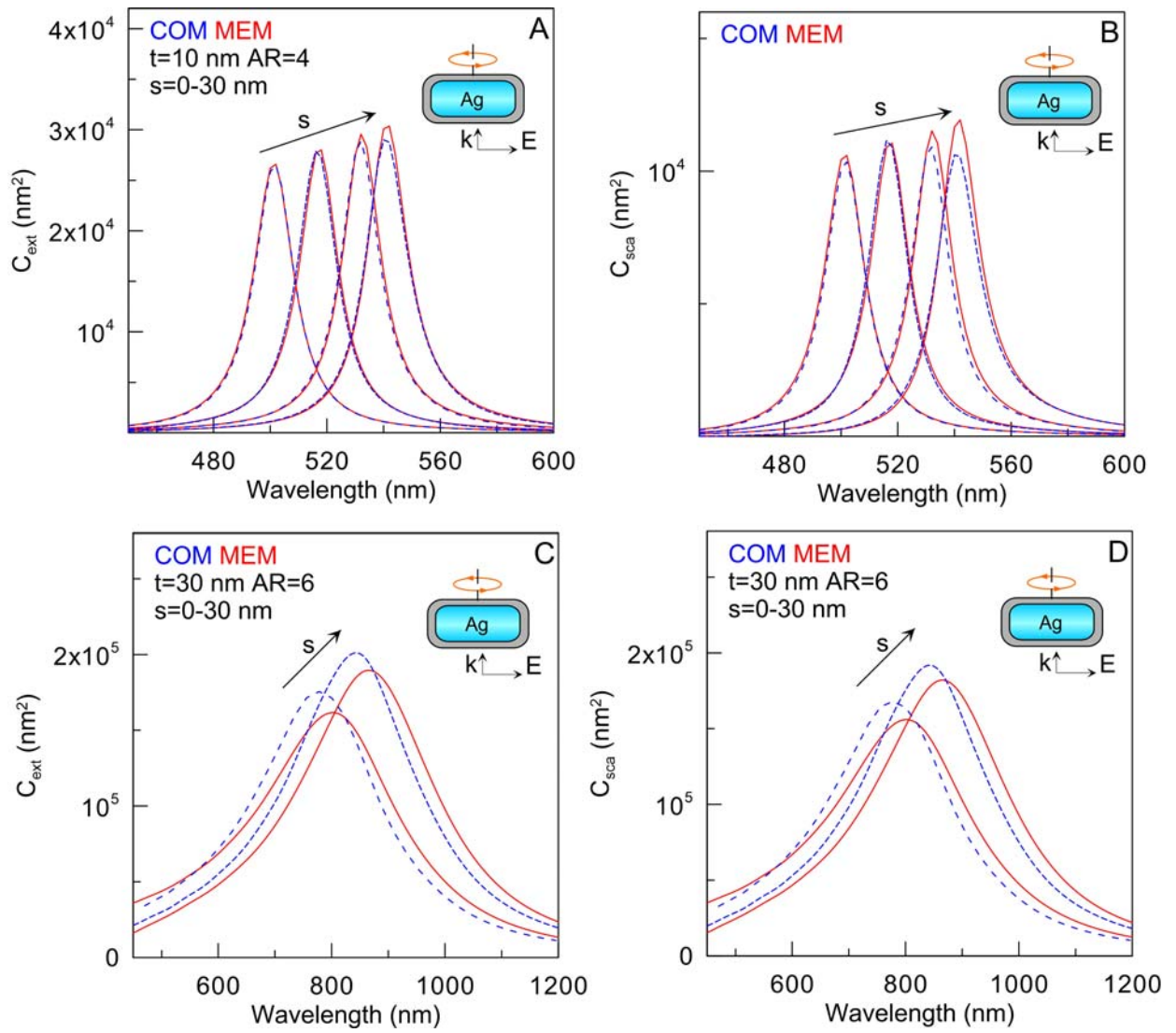


**Figure S11.** Extinction (A, C) and scattering (B, D) spectra of silver bare and coated nanodisks were calculated using MEM (red lines) and COMSOL (blue dashed lines). The particle thickness is  $L = 10$  nm (A, B) and  $30$  nm (C, D); their aspect ratios are  $4$  (A, B) and  $6$  (C, D). The coating thicknesses are  $0, 3, 10$  and  $30$  nm (A, B) and  $0, 30$  nm (C, D); the coating refractive index is  $1.5$ . The wave vector is directed along the disk axis.

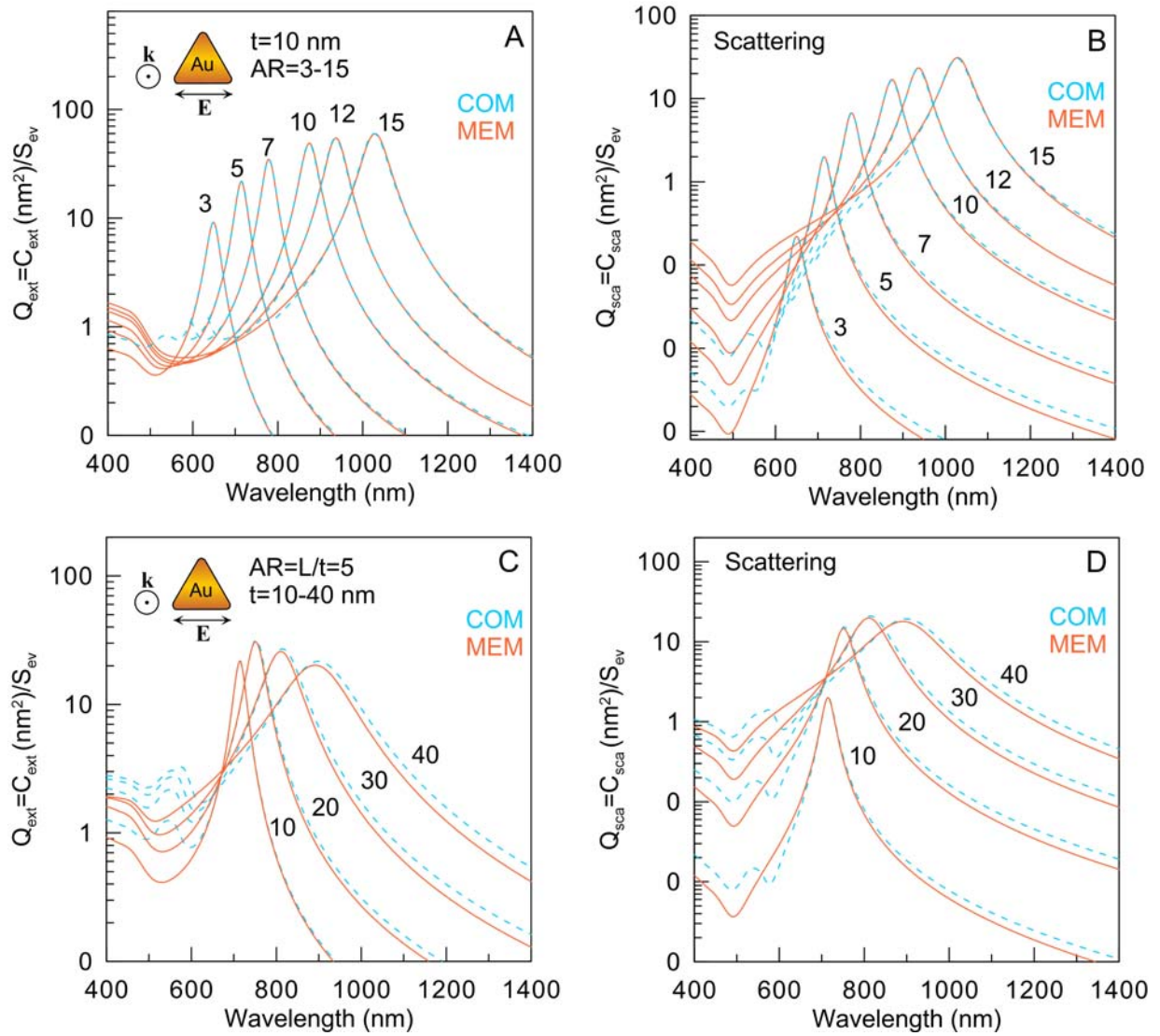


**Figure S12.** Comparison of extinction (A, C) and scattering (B, D) spectra calculated by COM (blue) and MEM (orange) for Au nanoprisms with a thickness of 10 nm and aspect ratios from 3 to 15 (A, B) and the aspect ratio of 5 and thicknesses from 10 to 40 nm (C, D). The electric field is directed along the major side (in-plane excitation). Note that MEM does not reproduce multipole peaks but approximates major plasmonic peaks well.

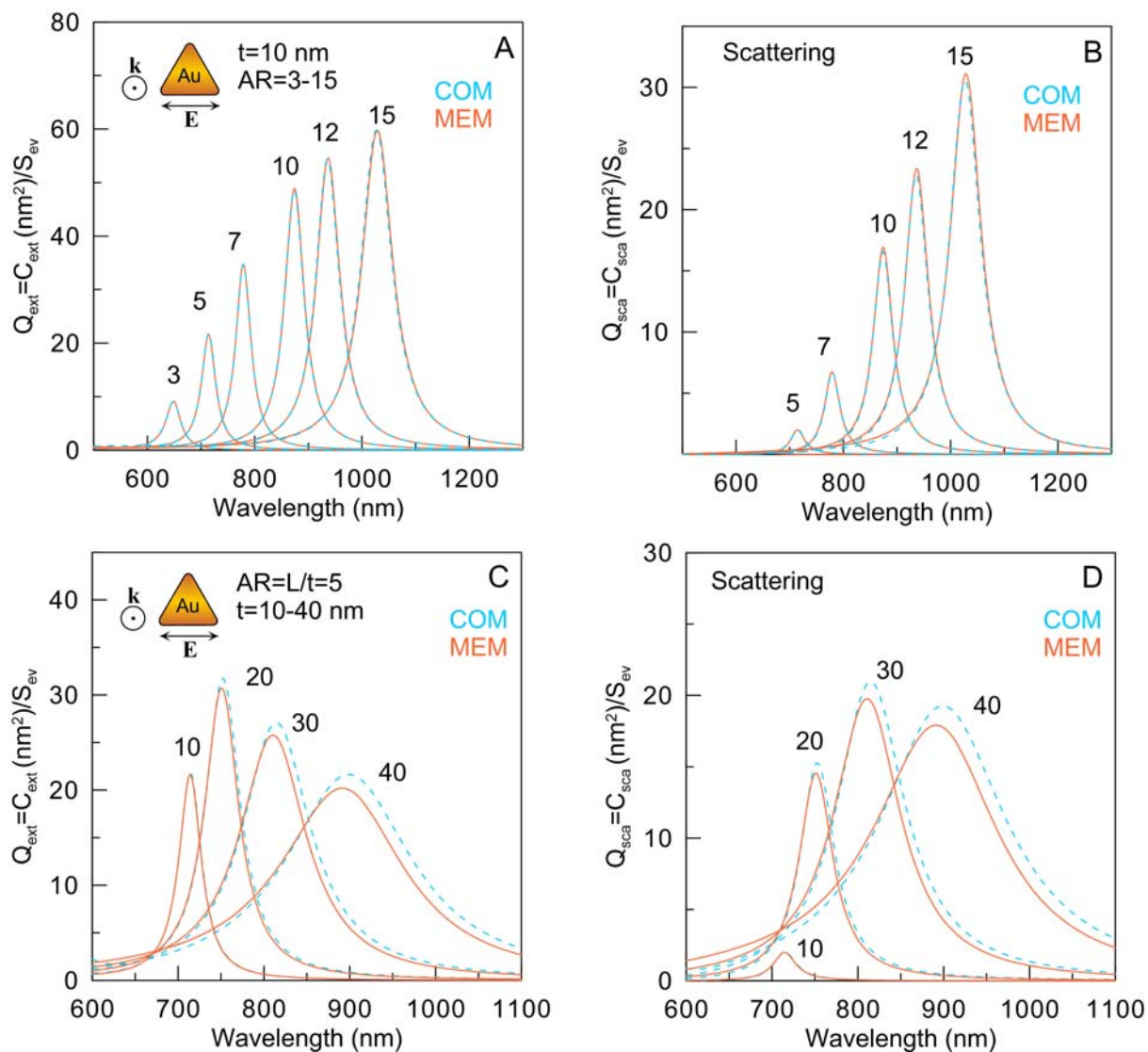


**Figure S13.** Same as in Figure S9 except for the linear ordinate scale. Note excellent agreement between COM and MEM spectra for thin nanoprisms (A, B) and some deviations for thicker ones (C, D).

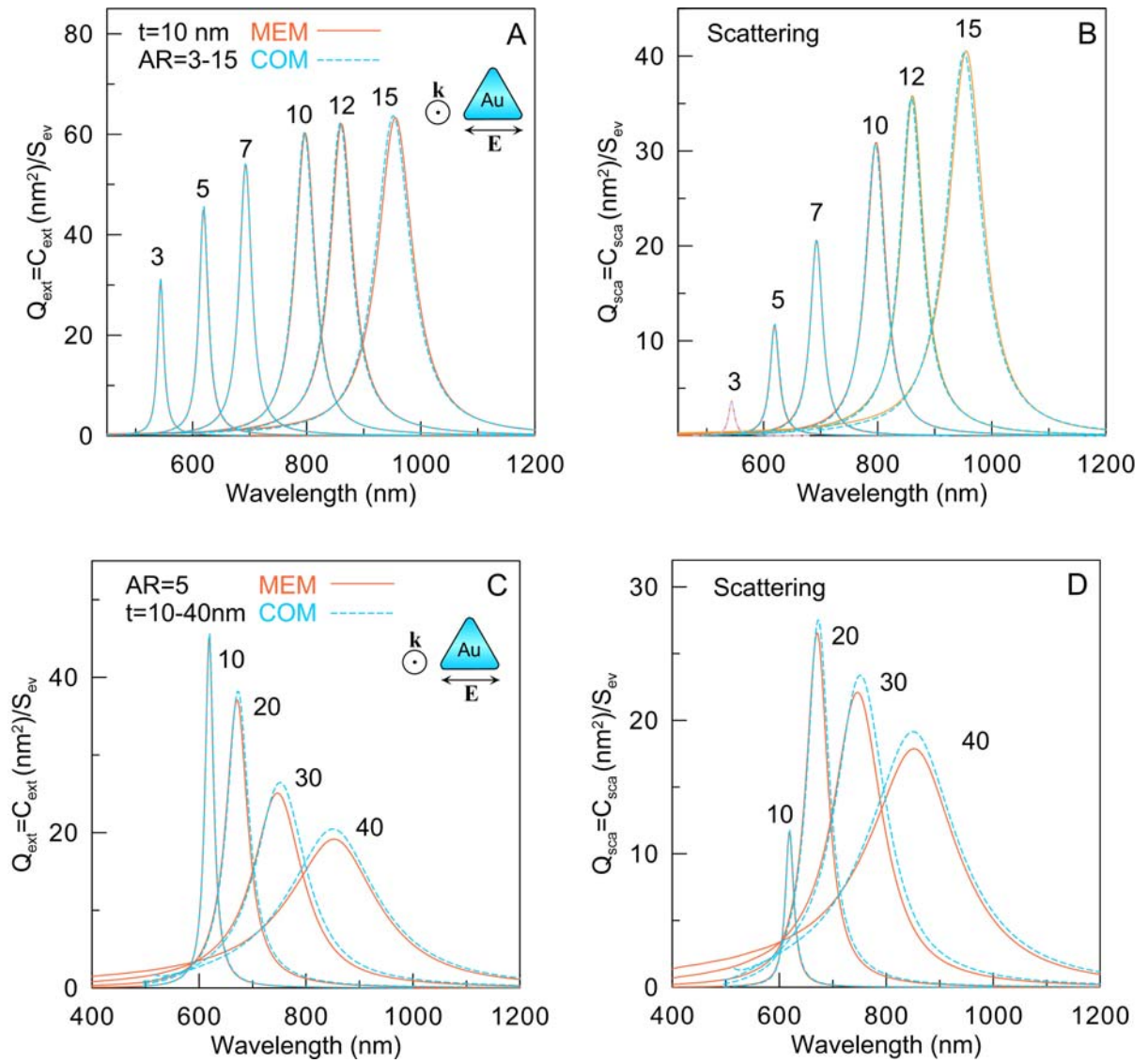


**Figure S14.** Comparison of extinction (A, C) and scattering (B, D) spectra calculated by COM (blue) and MEM (orange) for Ag nanoprisms with a thickness of 10 nm and aspect ratios from 3 to 15 (A, B) and the aspect ratio of 5 and thicknesses from 10 to 40 nm (C, D). The electric field is directed along the major side (in-plane excitation). Note that MEM does not reproduce multipole peaks (COM, not shown) but approximates major plasmonic peaks well.

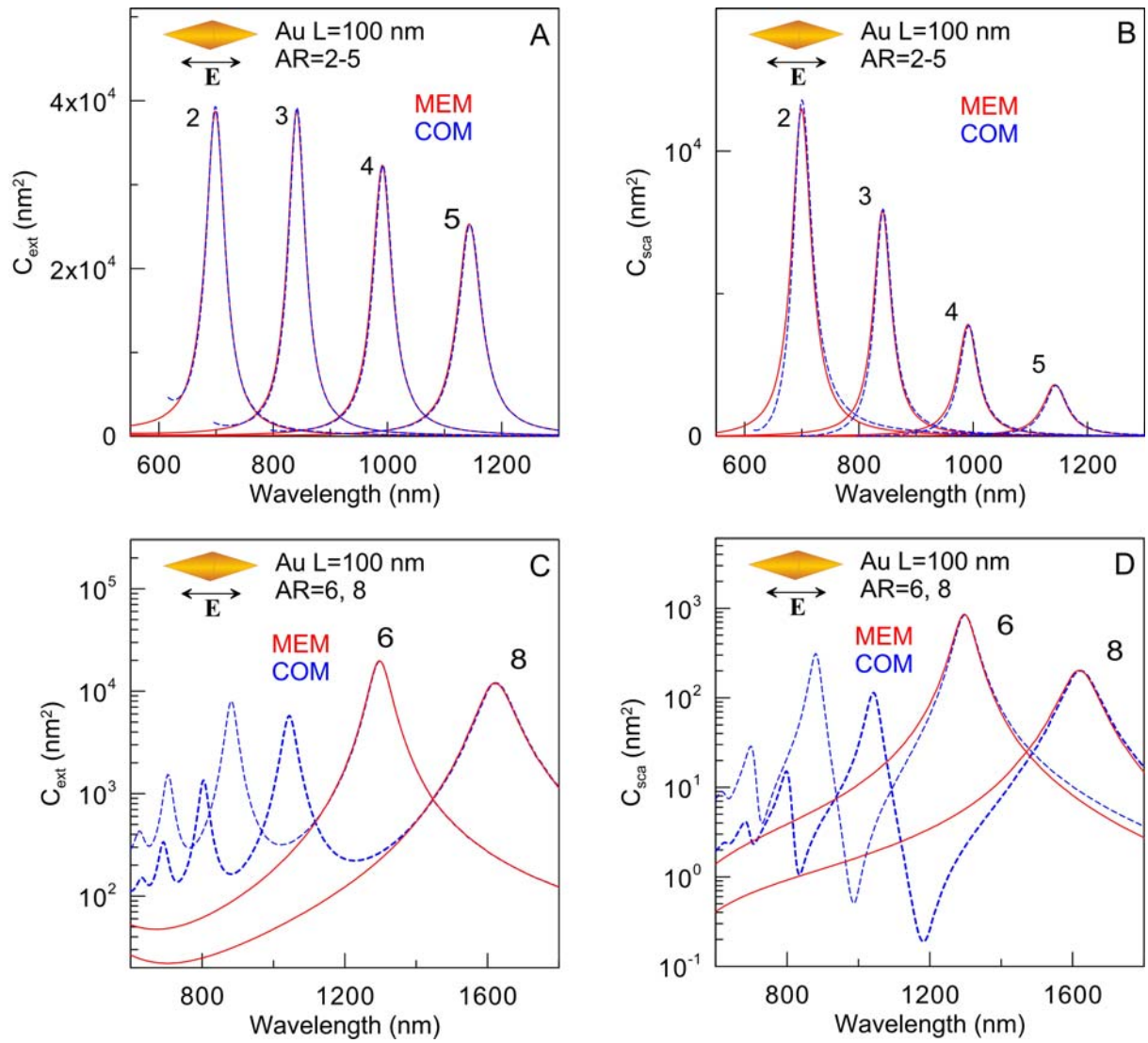


**Figure S15.** Comparison of extinction (A, C) and scattering (B, D) spectra calculated by COMSOL (blue) and MEM (red) for gold bicones of a fixed length of 100 nm and different aspect ratios from 2 to 8. Note that MEM approximation does not reproduce multipole peaks but reproduces the main dipolar resonance.

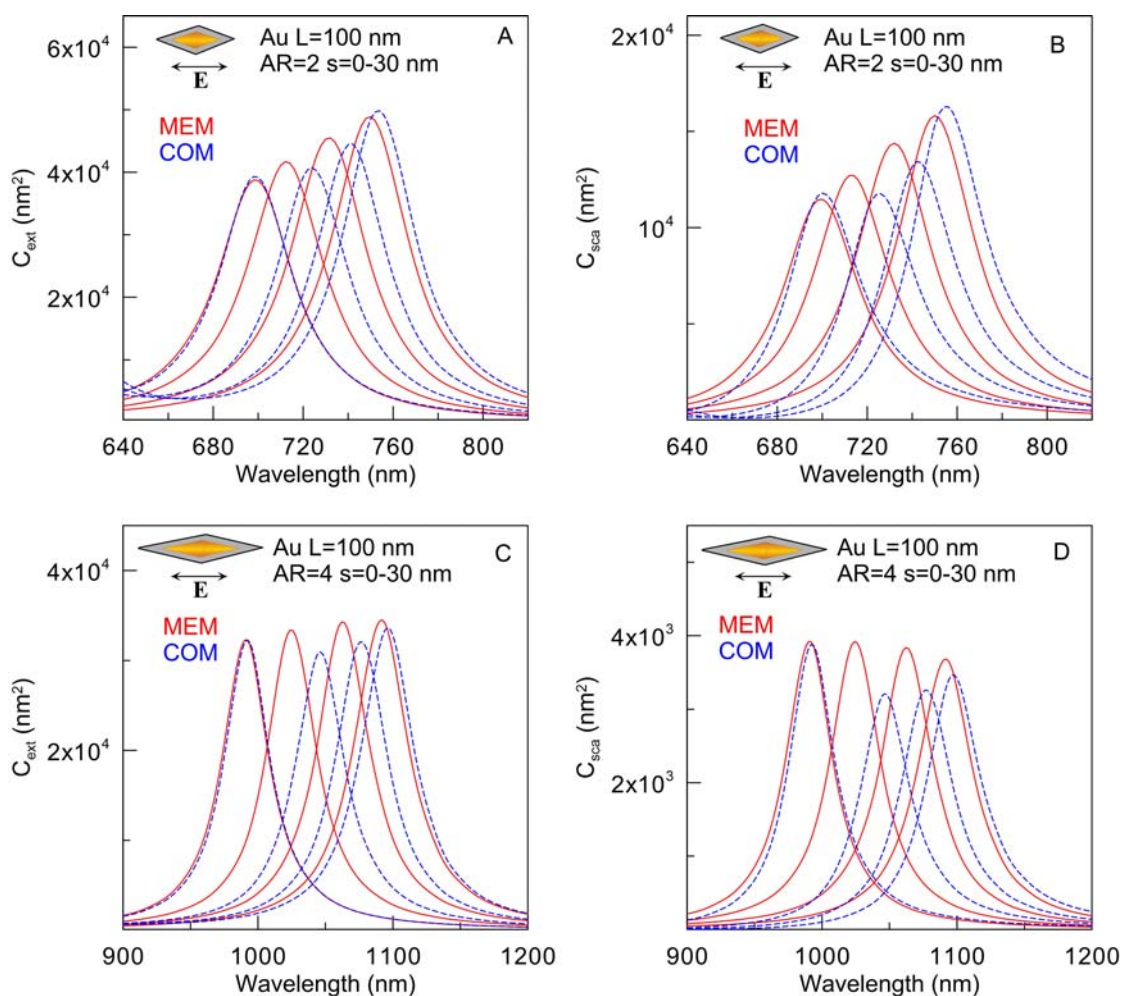


**Figure S16.** Comparison COMSOL and MEM extinction(A, C) and scattering (B, D) spectra calculated for coated gold bicones with a fixed core length of 100 nm, the aspect ratio of 2 (A, B) and 4 (C, D) and the coating shell thickness of 0, 3, 10, and 30 nm. Note the excellent agreement of spectra for the gold core and the significant difference between COMSOL and MEM spectra calculated for a small shell of 3 nm.

## References

1. Yu R., Liz-Marzán L. M., García de Abajo F. J. Universal analytical modeling of plasmonic nanoparticles. *Chem. Soc. Rev.* 2017, 46, 6710–6724.
2. Montaña-Priede J.L., Sánchez-Iglesias A., Mezzasalma S.A., Sancho-Parramon J., Grzelczak M. Quantifying shape transition in anisotropic plasmonic nanoparticles through geometric inversion. application to gold bipyramids. *J. Phys. Chem. Letters*, 2024, 15 (14), 3914–3922, DOI: 10.1021/acs.jpcllett.4c00582.